Physics of Fluids

Multiplexed Electrospray Emission on a Porous Wedge

Peter L. Wright[1, a)] and Richard E. Wirz[1, b)]
Mechanical and Aerospace Engineering Department, University of California, Los Angeles, 90095

(Dated: 23 November 2020)

Linear porous wedge electrospray emitters exhibit a discrete number of emission sites that naturally form during operation. An analytical model is developed to examine the behavior and spacing of these emission sites via the pressure variation in the porous fluid flow associated with the flow focusing to each emission site, which is coupled to the local electric field. The solution for site spacing and current is informed by empirical results with support from electric field modeling and investigation of porous media parameters. Emission site currents of up to 500 nA and site spacings of roughly 50 to 300 µm are predicted. Results from the model match well with experimental trends and provide further insight into the current and spacing of the discrete emission sites. These insights include: (1) for the investigated geometry, the total current can be estimated without taking into account the effects local to each emission site, (2) the wedge hydraulic resistance shows how the emitter output scales with emitter geometry and propellant properties, and (3) the emitted charge to mass ratio increases with applied electric field. Lastly, we present a physical description for how specific charge increases with the restorative pressure from the reservoir.

I. INTRODUCTION

Although electrospray devices traditionally use a capillary for fluid flow and electric field concentration, a sharpened porous medium can be used instead for these purposes. In porous media electrospray emitters, a working fluid flows through the porous medium to an emission surface, where the local electric field and fluid pressure allow for electrostatic emission of droplets or ions. Porous emitters have been used for aerosol generation,[1] mass spectrometry,[2] and electric space propulsion in both pointed tip[3,4] (including cones[5,6] and pyramids[7–9]) and wedge configurations.[10–15] A typical porous electrospray apparatus consists of an emitter substrate with a small characteristic pore size, coupled with a porous reservoir with a larger characteristic pore size. The small pore size of the emitter, compared to that of the reservoir, ensures that the emitter substrate stays wetted as liquid is sprayed from the system; liquid depletes from the reservoir to replace liquid in the emitter. An extractor electrode in close proximity to the emitter provides a strong electric field at the emitter when the emitter is charged, producing droplet and/or ion emission from the charged meniscus.[16]

A common approach to increasing the output of an electrospray device is to create many emission sites in parallel, a concept known as multiplexing. A straightforward approach to multiplexing is through manufacturing many individual features which will produce emission sites. Such a device requires high manufacturing consistency to produce uniform emission among sites. On the other hand, a wedge configuration for porous electrospray emitters allows for hundreds or thousands of discrete emission sites on a single emitter feature.[10,13] A sharp edge creates a region where the electric field is strong and nearly uniform. Along this edge, emission sites form due to the combined effects of the subsurface flow and local electric field. Rather than manufacturing individual features for each emission site, the wedge configuration allows for natural electrospray multiplexing through the interactions between emission sites. Due to these site to site interactions, the total output from a porous wedge electrospray emitter is reflective of both the emission site characteristics and site spacing. Experimental results from cone-shaped porous emitters have shown that multiple emission sites can form in a single high electric field region as voltage is increased.[17] Experimental observations of wedge-shaped emitters confirm emission from discrete sites along the sharp edge of the wedge.[18,19] Understanding the behavior of individual emission sites is critical to accurate estimation of device performance and lifetime.[20]

Multiple approaches exist for reducing the detrimental effects associated with the emission at the ends of the wedge, or 'edge effects.'[11] The increased sharpness at the end of the wedge increases the electric field in this region. One approach for mitigating edge effects is replacing the linear wedge with an annular wedge to eliminate the ends of the wedge segment;[11] another approach is to widen the extractor aperture at the ends in order to reduce the electric field in these regions.[15] A properly designed emitter using any of these approaches will mitigate off-nominal emission at wedge endpoints such that the majority of emission is characterized by emission in the uniform field region. Understanding the emission behavior in this uniform field region is crucial to understanding the behavior of the porous wedge electrospray device.

To investigate behavior and properties related to emission site spacing, this study develops a simplified model by considering the porous flow to each emission site. The applied electric field creates a pressure minimum at each emission site. The transition of the uniform upstream flow to individual flow cells at the emission surface causes a saddle point in the pressure at the stagnation points between emission sites. The coupling of the local electric field produced by each emission site with the fluid pressure at the surface of the porous medium causes the emission site spacing to change with applied electric field and reservoir pressure. A diagram of emission sites on the wedge is shown in Fig. 1c, based on figura-

a)Electronic mail: plloydwright@ucla.edu.
b)Electronic mail: wirz@ucla.edu

tive diagrams[13] and experimental results.[17–19] Emission sites are assumed to lie on the midplane of the emitter throughout; plume measurements indicate that emission sites

The objective of this research is to investigate the electric field and subsurface flow phenomena responsible for emission site current and spacing on the surface of a linear edge porous electrospray emitter. The uniform region of the wedge emitter, i.e. away from the ends, is considered for this investigation. The analysis is performed for low Reynolds number porous flow of superposed primary and secondary flows. The electric field caused by neighboring sites is simplified to produce analytical relations for the effect of these sites on fluid pressure in the porous medium. Experimental results from Courtney and Shea[10] are used to validate analytical results.

II. POROUS FLOW

For flow in porous media, both Darcy's law, $\vec{u} = -\frac{k}{\mu}\nabla P$, and continuity, $\nabla \cdot \vec{u} = 0$, are applicable. $\vec{u}$ is the fluid velocity, P is pressure, k is the porous permeability, and μ is the fluid viscosity. This form of Darcy's law is valid for low Reynolds number, i.e. $Re < 1$, where inertial effects can be neglected.[21] The Reynolds number is described as $Re = \rho u d/\mu$, where ρ is the fluid density, and d is the particle size in the porous medium.[21] Darcy's law and continuity are combined to show that the Laplacian of pressure is zero for low Re porous flows: $\nabla^2 P = 0$. As such, the flow can be decomposed into a primary and secondary flow for ease of solving and the solutions can be superposed into a new solution. We consider a primary flow that describes the net flow from the base of the emitter and a secondary flow that describes the local flow variation into discrete flow cells at each emission site, as shown in Fig. 1. For clarity in describing each flow, fluid velocity and pressure are denoted by a p-subscript for the primary flow and by an s-subscript for the secondary flow.

The geometry for the flow is a porous wedge of a specified angle, θ_w, with an upstream radius, R_1, and a downstream radius, R_2. The upstream radius is defined by the normal distance from the base of the wedge to the virtual apex of the wedge. The downstream radius is assumed as the distance from the virtual apex of the wedge to the midplane surface of the emission surface, as shown in Fig. 2. Assuming the downstream boundary condition in this way pulls the low pressure boundary condition closer to the virtual apex of the wedge and spreads the condition over a larger area. As a result, the fluid flow of the modelled emitter departs from that of a physical device near the emission site. The exposed surface of the physical device intersects with the assumed fluid flow domain for $R_2 < r < R_{2+}$, where R_{2+} is the distance from the virtual apex of the wedge to where the convex emission surface intersects with the sides of the wedge at $\theta = \pm\theta_w/2$. In this region of a physical device, the flow is not necessarily axisymmetric. While assuming a convex surface at R_2 approximates the flow to the emission surface, it is likely an underestimate of the hydraulic resistance to the emission site for the above reasons. For an emitter wedge half-angle of 30°, R_2 is equal to the radius of curvature of the emission surface, R_{emit}, and R_{2+} is twice R_2. The porous medium is assumed to be isotropic and uniformly characterized by its permeability.

The electric field is also decomposed into both primary and secondary electric fields, using the same subscript notation as previously described for the flow field. The primary electric field is produced by the extraction electrode on the surface of the emitter when no emission sites are present. The secondary electric field is produced by the charge concentration near each emission site. The medium for the electrostatic region is vacuum and the space charge is neglected outside of the plume and cone at each emission site, so the electric potential, ϕ, in the region is described by $\nabla^2\phi = 0$. Because the electric potential is described by Laplace's equation, superposition of solutions in this region is valid.

The pressure boundary conditions for flow through the emitter are the emission pressure at the emission sites on the tip of the wedge and the Laplace pressure provided by the meniscus in the reservoir. Both of these pressure conditions are below the ambient pressure, causing the fluid throughout the porous medium to be below ambient pressure. For the working fluid to leave the porous medium, the electric pressure at the surface must exceed the Laplace pressure provided by the reservoir. The emission surface represents the highest electric field region of the emitter, so it is expected that the electric field is insufficient to cause the working fluid from escaping the porous emitter away from the emission surface. As a result, there is no fluid velocity in the normal direction to exposed porous surfaces, such as the limits of the wedge at $\theta = \pm\theta_w/2$ where $u_\theta = 0$. Also, because there is a free meniscus at $\theta = \pm\theta_w/2$, the interface is considered to be a free-slip boundary condition. The result from these two conditions is that there is no flow in the θ-direction and no dependence on θ for flow in the r- and z-directions, so the dependence on the flow on θ can be ignored.

The primary flow describes the net flow from the porous reservoir to the emission site. The flow rate through the emitter, Q_p, is defined by the single emission site flow rate, Q_{site}, the spacing between sites, λ, and the emitter length, L, as follows:

$$Q_p = \frac{LQ_{site}}{\lambda}. \tag{1}$$

There is no pressure gradient in the z- or θ-directions for the primary flow, so $u_{p,z} = u_{p,\theta} = 0$ and the flow velocity in the r-direction is described by the flow rate and cross-sectional area, $A(r)$:

$$u_{p,r} = -\frac{Q_p}{A(r)} = -\frac{Q_{site}}{\theta_w r\lambda}. \tag{2}$$

Applying Darcy's law to flow in the radial direction determines the pressure field for the primary flow:

$$P_p(r) = \frac{\mu Q_{site}}{k\theta_w\lambda}\ln(r) + C_1, \tag{3}$$

where C_1 is a constant.

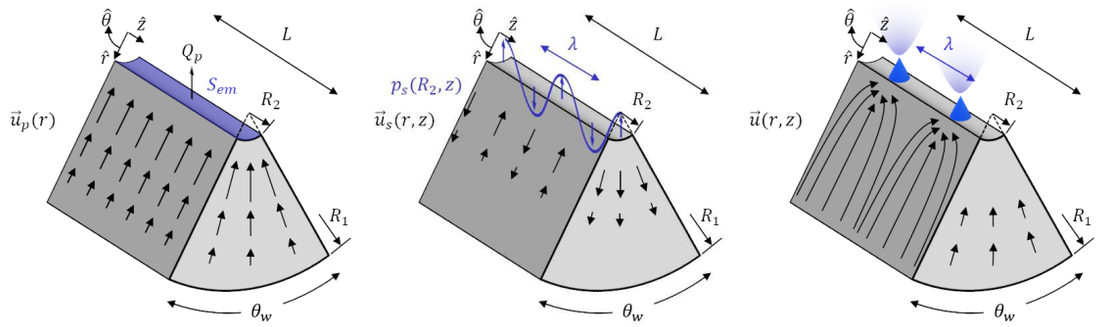

(a) (b) (c)

FIG. 1: The wedge emitter geometry, with the a) primary flow, b) secondary flow, and c) combined flow with discrete emission sites.

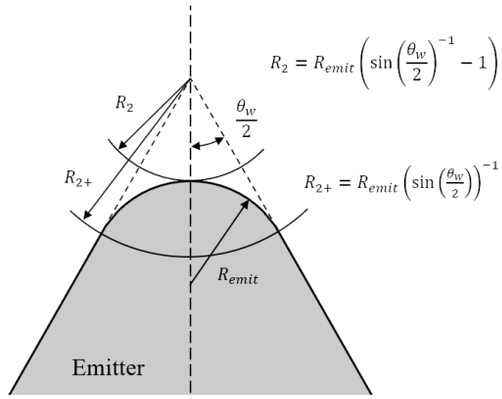

FIG. 2: The convex emission surface with a radius of R_{emit} is assumed as a concave surface with radius R_2 to maintain axisymmetry in the porous flow domain. Fluid flow in a physical device may depart from the predicted behaviour between R_2 and R_{2+}.

The secondary flow describes the spatially periodic separation of the net flow into individual emission sites, assuming a regular variation of the pressure in the z-direction. This condition causes flow in the r- and z-directions localized to the emission surface while assuming uniformity in the θ-direction. Pressure in the secondary flow is solved for by assuming a separation of variables solution with components $M(r)$ and $N(z)$ for the axisymmetric form of $\nabla^2 P = 0$. The equation is solved by finding the solution to the eigenvalue problem:

$$\frac{\frac{1}{r}\frac{\partial}{\partial r}\left(r\frac{\partial M}{\partial r}\right)}{M} = -\frac{\frac{\partial^2 N}{\partial z^2}}{N} = \alpha^2, \tag{4}$$

where α is the eigenvalue. The solutions to these equations are the zeroth-order modified Bessel functions of the first and second kind for $M(r)$ and an oscillatory solution for $N(z)$:

$$P_s(r,z) = \left[C_2 K_0(\alpha r) + C_3 I_0(\alpha r)\right] e^{i\alpha z}, \tag{5}$$

where I_0 and K_0 are the modified Bessel Functions of the first and second kind, respectively, and C_2 and C_3 are constant coefficients. The wavelength for the pressure oscillation is defined by the emission site separation distance, $\lambda = 2\pi/\alpha$. To simplify Eq. 5, the emission site spacing is assumed to be small compared to the base of the wedge, i.e. $\lambda \ll 2\pi R_1$, such that the pressure variation within the wedge due to the I_0 term is negligible. With these assumptions, the secondary flow pressure solution can be alternatively expressed as:

$$P_s(r,z) = C_2 K_0\left(\frac{2\pi r}{\lambda}\right) e^{\frac{2\pi i z}{\lambda}}. \tag{6}$$

For cases where a small λ assumption cannot be made, the pressure due to the secondary flow is derived in Appendix I.

As shown in Fig. 1, the primary and secondary flows are coupled such that stagnation points exists at the midpoint between each emission site. At these points the primary and secondary flows are equal and opposite. At the stagnation point, $(r,z) = (R_2, n\lambda)$ where n is an integer, the pressure gradients in the r-direction for the primary and secondary flows are equal and opposite:

$$\frac{\mathrm{d}}{\mathrm{d}r}P_p(R_2) = -\frac{\partial}{\partial r}P_s(R_2, n\lambda). \tag{7}$$

Substituting Eqs. 3 and 6 into Eq. 7 and simplifying yields:

$$\frac{\mu Q_{site}}{k\theta_w R_2 \lambda} = \frac{2\pi C_2}{\lambda} K_1\left(\frac{2\pi R_2}{\lambda}\right). \tag{8}$$

C_2 is used to enforce the stagnation point when superposing the primary and secondary flows:

$$C_2 = \frac{\mu Q_{site}}{2\pi k\theta_w R_2} \frac{1}{K_1\left(\frac{2\pi R_2}{\lambda}\right)}. \tag{9}$$

The combined pressure solution is simply a superposition of the primary and secondary flows:

$$P(r,z) = \frac{\mu Q_{site}}{k\theta_w}\left(\frac{1}{\lambda}\ln(r) + \frac{1}{2\pi R_2}\frac{K_0\left(\frac{2\pi r}{\lambda}\right)}{K_1\left(\frac{2\pi R_2}{\lambda}\right)} e^{\frac{2\pi i z}{\lambda}}\right) + C_1. \tag{10}$$

III. APPLYING BOUNDARY CONDITIONS

The total current output of the emitter is obtained by equating the applied pressure difference to the decrease in pressure associated with the flow through porous medium. The applied pressure difference, from the base of the wedge to the emission surface, is from $r = R_1$ to $(r,z) = (R_2,(2n+1)\lambda/2)$.

The effect of the secondary flow is negligible for $r >> R_2$, so the pressure at the wedge base is uniform in the z-direction and approximated as the reservoir pressure. The pressure drop due to flow through the porous medium, ΔP_{por}, is solved as:

$$\Delta P_{por} = \frac{\mu Q_{site}}{k\theta_w}\left(\frac{1}{\lambda}\ln\left(\frac{R_2}{R_1}\right) - \frac{1}{2\pi R_2}\frac{K_0\left(\frac{2\pi R_2}{\lambda}\right)}{K_1\left(\frac{2\pi R_2}{\lambda}\right)}\right). \quad (11)$$

The right side of Eq. 11 represents the single flow cell hydraulic resistance multiplied by the single flow cell flow rate.

The reservoir pressure is approximated by the Laplace pressure, or capillary pressure, from a meniscus at a fully-wetted pore upstream in the reservoir[21,22] and the emission surface pressure is approximated by the Maxwell pressure supplied by the magnitude of the local primary extraction electric field, E_p.[5,23,24] The applied pressure difference from the fluid reservoir to emission site, ΔP_{app}, is:

$$\Delta P_{app} = \frac{4\gamma}{D_{res}} - \frac{1}{2}\varepsilon_0 E_p^2, \quad (12)$$

where γ is the fluid surface tension coefficient, D_{res} is the characteristic reservoir pore size, and ε_0 is the permittivity of free space. Furthermore, the individual emission site flow rate is replaced by the individual emission site current, I_{site}, the fluid density, ρ, and the mean specific charge of emission products, q/m:

$$Q_{site} = \frac{I_{site}}{\rho}\frac{m}{q}. \quad (13)$$

Applying these conditions and setting the porous flow pressure drop to be equal to the applied pressure difference, an expression for the pressure balance for a linear edge electrospray emitter is developed:

$$\frac{\mu I_{site}}{k\rho\theta_w}\frac{m}{q}\left(\frac{1}{\lambda}\ln\left(\frac{R_2}{R_1}\right) - \frac{1}{2\pi R_2}\frac{K_0\left(\frac{2\pi R_2}{\lambda}\right)}{K_1\left(\frac{2\pi R_2}{\lambda}\right)}\right) = \frac{4\gamma}{D_{res}} - \frac{1}{2}\varepsilon_0 E_p^2. \quad (14)$$

To simplify Eq. 14, all λ-dependent terms are combined into a single function, F:

$$F(\lambda,R_1,R_2) = \frac{1}{\lambda}\ln\left(\frac{R_2}{R_1}\right) + \frac{1}{2\pi R_2}\frac{K_0\left(\frac{2\pi R_2}{\lambda}\right)}{K_1\left(\frac{2\pi R_2}{\lambda}\right)}. \quad (15)$$

F can be expressed as the sum of its terms:

$$F = F_1 + F_2 : \quad (16)$$

$$F_1 = \frac{1}{\lambda}\ln\left(\frac{R_2}{R_1}\right), \quad (17)$$

$$F_2 = \frac{1}{2\pi R_2}\frac{K_0\left(\frac{2\pi R_2}{\lambda}\right)}{K_1\left(\frac{2\pi R_2}{\lambda}\right)}. \quad (18)$$

F, F_1, and F_2 are plotted with respect to the site spacing, λ, in Fig. 3. For the geometry from Courtney and Shea,[10] F_1 and F_2 are equal for $\lambda = 2.56$ mm. For $\lambda \ll 2.56$ mm, F_1 dominates F, so F_2 can be ignored. For the case where many emission sites exist over the length of the emitter, L, i.e. $\lambda \ll L$, F can be approximated as F_1, and Eq. 14 can be simplified as:

$$\frac{\mu I_{site}}{k\rho\theta_w\lambda}\frac{m}{q}\ln\left(\frac{R_2}{R_1}\right) \approx \frac{4\gamma}{D_{res}} - \frac{1}{2}\varepsilon_0 E_p^2. \quad (19)$$

The small site spacing approximation is possible due to the argument of the Bessel terms in Eq. 18 being below 1, i.e. for the condition $\lambda \leq 2\pi R_2 \approx 125\,\mu$m.

The ratio of total emitter current, I_{total}, to the emitter length, L, is equal to the ratio of the single emission site current to the emission site spacing:

$$\frac{I_{total}}{L} = \frac{I_{site}}{\lambda}. \quad (20)$$

Equation 20 allows Eq. 14 to be solved for the total current from the electrospray device:

$$I_{total} \approx \frac{\rho k\theta_w L}{\mu\ln\left(\frac{R_2}{R_1}\right)}\frac{q}{m}\left(\frac{4\gamma}{D_{res}} - \frac{1}{2}\varepsilon_0 E_p^2\right). \quad (21)$$

For a given working fluid and emitter, all parameters contributing to I_{total} in Eq. 21 are effectively constant except for specific charge and electric field.

IV. ELECTROSTATIC REGION

Similarly to the porous flow solutions, the electric field is separated into primary and secondary electric fields. The primary electric field represents the electric field due to the voltage difference between emitter and extractor electrodes, while

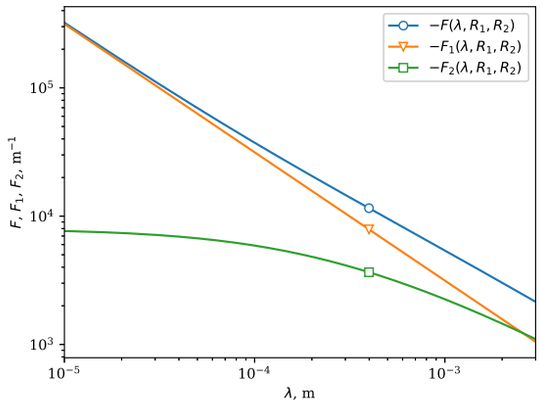

FIG. 3: F and its terms as a function of emission site spacing for $R_1 = 465\,\mu$m and $R_2 = 20\,\mu$m.

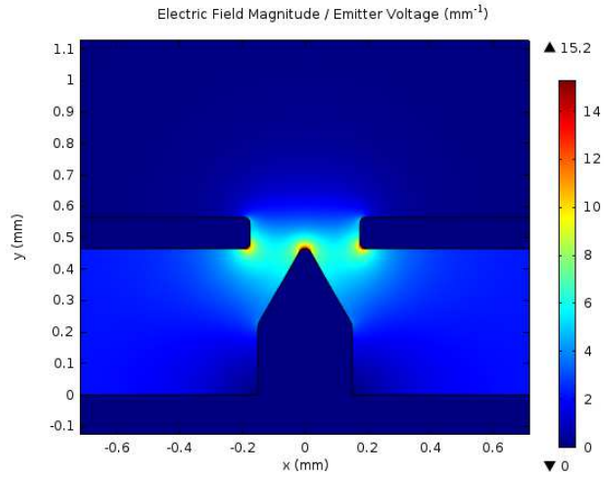

FIG. 4: Simulation of the normalized electric field produced by the wedge emitter used to estimate the primary electric field.

the secondary field describes the effect of charge accumulation due to each emission site.

The electric field applied to the emitter reduces the pressure at the emission surface, driving flow through the porous medium. In this effort, we use the electric field in the absence of Taylor cones to estimate the pressure at the emission surface. Even though the electric field on the cone increases drastically towards the apex, the curvature of the meniscus increases in response.[25,26] Because the electrostatic and surface tensions effects are in equilibrium, we expect that the pressure difference due to varying electric field along the meniscus can be neglected. Thus, the applied electric field provides a reasonable basis for estimating the pressure at the emission site.[24]

Recombining the primary and secondary solutions for the electric field introduces challenges with regard to how boundary conditions should be maintained. Addition of the two electric field solutions superposes the electric potential from each solution throughout the electrostatic region. Near to the emission sites, the electric field from the cone causes the isopotential surface at the extraction voltage to extend past the emission surface.

Because the emission site is of the same order as the emission site to extractor electrode distance (175 µm) over the operating conditions of the emitter, adding the secondary electric field to the primary field overestimates the voltage on the emitter surface and extractor electrode to approximately the same margin. Results for the emission site spacing as a function of voltage and reservoir pores size are shown in Fig. 9. Although approximating the electric fields in the manner described may not maintain the correct potential at each electrode, the important quality to maintain is the voltage difference between the emitter and extractor electrodes. By maintaining the extraction voltage in this way, the superposition of primary and secondary electric fields serves as a useful way to estimate the electric field from emission sites while maintaining the electric field produced by the extractor electrode.

The primary electric field is linearly related to the emitter voltage by a parameter C_E, which is a function of the emitter and extractor electrode geometry:[5]

$$E_p = C_E V_{emit}. \tag{22}$$

C_E has been determined with an electrostatic solver for the geometry defined in Courtney and Shea,[10] as shown in Fig. 4, yielding a value of 15.3 mm^{-1} for a uniform emitter tip radius of 20 µm.

The startup voltage condition, V_{start}, can be found by setting $\Delta P_{app} = 0$, and solving Eqs. 12 and 22 for emitter voltage:

$$V_{start} = \frac{1}{C_E}\sqrt{\frac{8\gamma}{\varepsilon_0 D_{res}}}. \tag{23}$$

To find the emission site spacing and single emission site current, the coupled effects of the secondary electric field and secondary flow solution must be considered. To ensure a valid secondary solution, there must be no pressure difference across the meniscus, i.e. the Maxwell pressure and static pressure must be in equilibrium at the interface. For ease of calculation, the pressures are equalized at the stagnation point between adjacent emission sites. The secondary electric field is approximated by a point charge representing the charge within each Taylor cone and a semi-infinite line of charge representing each plume of charged particles emitted from the Taylor cone at each emission site. At each stagnation point, only the two nearest-neighbor emission sites are considered when estimating the electric field.

The linear charge density of the simplified plume, σ_l, is equal to the ratio of the emitted current to particle exit velocity, c. The exit velocity can be estimated through conservation of energy:

$$\sigma_l = \frac{I_{site}}{c} = I_{site}\sqrt{\frac{m}{2V_{emit}q}}, \tag{24}$$

where V_{emit} is the emitter voltage. The electric field imposed by two plumes on the stagnation point between two emission

sites, $E_{s,1}$, is twice the electric field imposed in the upstream direction by a single semi-infinite line of charge:

$$E_{s,1}(R_2, n\lambda) = \frac{2\sigma_l}{4\pi\varepsilon_0\left(\frac{\lambda}{2}\right)} = \frac{I_{site}}{\pi\varepsilon_0\lambda}\sqrt{\frac{m}{2V_{emit}q}}. \tag{25}$$

The electric field produced by each Taylor cone is simplified to a point charge at its apex. We assume that the size of the Taylor cone scales with a characteristic length, which is assumed to be the radius of curvature of the meniscus required to compensate for the negative pressure applied by the primary electric field. Thus, the normal distance from the tip of the wedge to the assumed point charge is estimated to be equal to the characteristic length of the cone.

$$a = \frac{4\gamma}{\varepsilon_0 E_p^2}. \tag{26}$$

The meniscus formed by a Taylor cone with negative back-pressure has been determined to have a concave cross-section[27,28] that departs from the 49.3° half-angle cone determined by Taylor.[25] The total charge and shape of a charged meniscus at a negative-pressure emission site are an ongoing research topic,[29] so for the sake of simplicity and the purpose of this investigation, the specific geometry of the emission site is ignored in favor of a simplified representation of the Taylor cone size.

The connection between fissioning charged droplets and Taylor cones has been previously noted.[30] The Taylor cone is approximated as half of a droplet with radius a undergoing Rayleigh fission. Thus, the charge contained in the Taylor cone, q_{TC}, is approximated as half of the charge required for a droplet to fission by the Rayleigh instability,[31,32] which is simplified with Eq. 26 as:

$$q_{TC} = \frac{1}{2}\sqrt{64\pi^2\varepsilon_0\gamma a^3} = \frac{32\pi\gamma^2}{\varepsilon_0 E_p^3}. \tag{27}$$

Experimentally, droplet fission has been observed at 70 to 90% of the Rayleigh limit[33,34] and the charge of a Taylor cone has been estimated as low as 57% of the Rayleigh limit;[35] for simplicity, emission below the Rayleigh limit is ignored as part of this investigation.

The electric field produced by 2 point charges at adjacent Taylor cones on the stagnation point is determined using Coulomb's law and Eqs. 26 and 27:

$$\begin{aligned} E_{s,2}(R_2, n\lambda) &= \frac{2aq_{TC}}{4\pi\varepsilon_0}\left(a^2 + \frac{\lambda^2}{4}\right)^{-\frac{3}{2}} \\ &= \frac{64\gamma^3}{\varepsilon_0^3 E_p^5}\left(\left(\frac{4\gamma}{\varepsilon_0 E_p^2}\right)^2 + \frac{\lambda^2}{4}\right)^{-\frac{3}{2}}. \end{aligned} \tag{28}$$

The electric field from the cone and from the plume are superposed to determine the Maxwell pressure on the meniscus at the midpoint between emission sites:

$$E_s(R_2, n\lambda) = E_{s,1}(R_2, n\lambda) + E_{s,2}(R_2, n\lambda): \tag{29}$$

$$\begin{aligned} E_s(R_2, n\lambda) &= \frac{I_{site}}{\pi\varepsilon_0\lambda}\sqrt{\frac{m}{2V_{emit}q}} \\ &+ \frac{64\gamma^3}{\varepsilon_0^3 E_p^5}\left(\left(\frac{4\gamma}{\varepsilon_0 E_p^2}\right)^2 + \frac{\lambda^2}{4}\right)^{-\frac{3}{2}}. \end{aligned} \tag{30}$$

If the height of the Taylor cone is assumed to be much smaller than the distance between neighboring emission sites, then the distance from the apex of the Taylor cone to the stagnation point can be approximated as half the emission site spacing. Results with this approximation are designated in Figs. 9 and 10 as using the small angle approximation for the secondary electric field. Additionally, the electric field from the plume is assumed to be negligible compared to that from the cone; when operating in vacuum, there is little resistance on emitted particles to cause high charge density in the plume compared to the meniscus of the cone. A quantitative comparison of the electric fields from the cone and plume is presented in Section VI as further justification of this assumption. With these assumptions, Eq. 30 can be simplified as:

$$E_s(R_2, n\lambda) = \frac{64\gamma^3}{\varepsilon_0^3 E_p^5}\left(\frac{\lambda^2}{4}\right)^{-\frac{3}{2}} = \frac{2^9\gamma^3}{\varepsilon_0^3 E_p^5 \lambda^3}, \tag{31}$$

which results in a Maxwell pressure of:

$$\Delta P_{s,E} = \frac{1}{2}\varepsilon_0\left(\frac{2^9\gamma^3}{\varepsilon_0^3 E_p^5\lambda^3}\right)^2 = \frac{2^{17}\gamma^6}{\varepsilon_0^5 E_p^{10}\lambda^6}. \tag{32}$$

The pressure difference from the emission site to the midpoint between emission sites is determined from Eqs. 6 and 9 as:

$$\Delta P_{s,u} = \frac{\mu I_{site}}{\pi\rho k\theta_w R_2}\frac{m}{q}\frac{K_0\left(\frac{2\pi R_2}{\lambda}\right)}{K_1\left(\frac{2\pi R_2}{\lambda}\right)}. \tag{33}$$

The secondary flow pressure difference and the Maxwell pressure from the secondary electric field are equated to enforce the static equilibrium condition for the full secondary flow and electric field solution:

$$\frac{\mu I_{site}}{\pi\rho k\theta_w R_2}\frac{m}{q}\frac{K_0\left(\frac{2\pi R_2}{\lambda}\right)}{K_1\left(\frac{2\pi R_2}{\lambda}\right)} = \frac{2^{17}\gamma^6}{\varepsilon_0^5 E_p^{10}\lambda^6}, \tag{34}$$

which in turn is simplified for I_{site} as:

$$I_{site} = \frac{2^{17}\pi\gamma^6}{\varepsilon_0^5 E_p^{10}\lambda^6}\frac{\rho k\theta_w R_2}{\mu}\frac{q}{m}\frac{K_1\left(\frac{2\pi R_2}{\lambda}\right)}{K_0\left(\frac{2\pi R_2}{\lambda}\right)}. \tag{35}$$

To solve for the emission site spacing as a function of applied electric field, Eq. 35 is substituted into Eq. 19 and simplified, yielding the following equation:

$$\frac{1}{\lambda^7}\frac{K_1\left(\frac{2\pi R_2}{\lambda}\right)}{K_0\left(\frac{2\pi R_2}{\lambda}\right)} = \frac{\varepsilon_0^5 E_p^{10}}{2^{17}\pi\gamma^6 R_2 \ln\left(\frac{R_2}{R_1}\right)}\left(\frac{4\gamma}{D_{res}} - \frac{1}{2}\varepsilon_0 E_p^2\right). \tag{36}$$

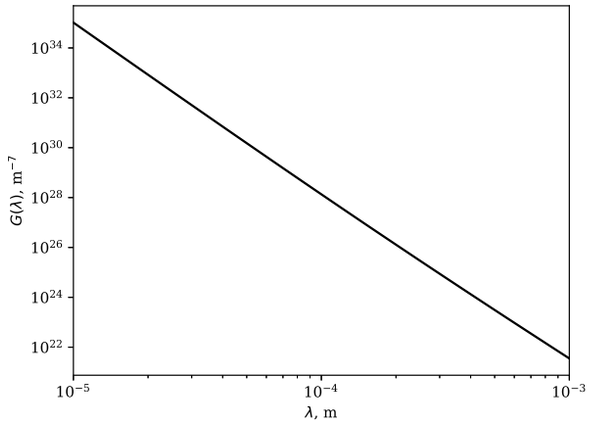

FIG. 5: $G(\lambda)$, which represents the left side of Eq. 36, plotted over the relevant range of λ.

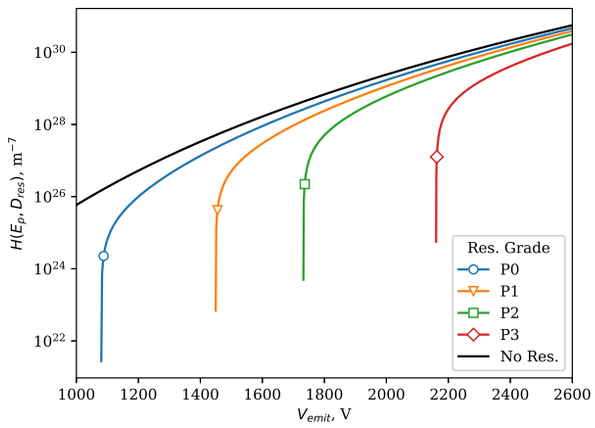

FIG. 6: $H(E_p, D_{res})$, which represents the right side of Eq. 36, plotted over the relevant range of emitter voltage.

The left and right sides of Eq. 36 can be expressed as $G(\lambda)$ and $H(E_p, D_{res})$ respectively, with fluid properties and emitter geometry remaining constant. $G(\lambda)$ and $H(E_p, D_{res})$ are plotted in Figs. 5 and 6, where H is plotted for the pore sizes assumed to represent each reservoir porous media grade. Evaluating Eq. 36 over the operating range of the device investigated has shown that small changes to E_p are roughly magnified twofold at nominal operating conditions, although the emission site spacing becomes increasing sensitive to changes in E_p when operated close to the startup voltage.

V. OPERATIONAL PARAMETERS

The mean specific charge of emitted species is assumed to scale with the specific charge of the Taylor cone from which

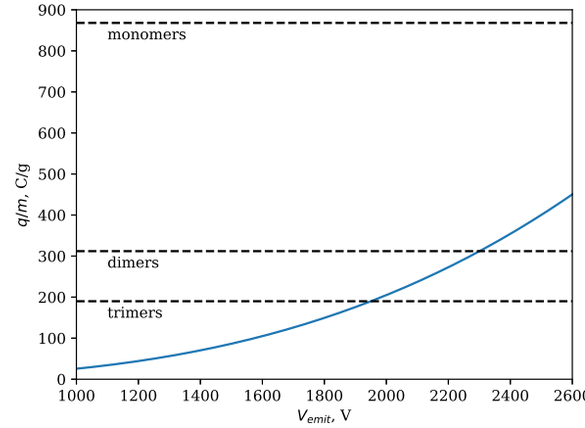

FIG. 7: The specific charge of emitter species as a function of emitter voltage, with the positive monomer, dimer, and trimer species for reference.

they originate:[36]

$$\frac{q}{m} \propto \frac{q_{TC}}{\rho a^3} \rightarrow \frac{q}{m} \propto \frac{1}{\rho}\frac{\gamma^2}{E_p^3}\left(\frac{E_p^2}{\gamma}\right)^3 = \frac{E_p^3}{\rho\gamma}. \tag{37}$$

An empirical constant A, with units of $\mathrm{C^4 s^4 m^{-6} kg^{-2}}$, is introduced to represent the effects of meniscus shape, relative permittivity, and all other relevant parameters. The specific charge of emitted species, q/m, is then treated as:

$$\frac{q}{m} = A\frac{E_p^3}{\rho\gamma}. \tag{38}$$

Courtney and Shea[10] show that the electrospray plume is dimer-dominated with little droplet emission when operating their emitter with a P5-grade reservoir at approximately 20 µA, or 312 C g^{-1} at an emitter voltage of approximately 2200 V. To match the specific charge of a dimer-dominated plume at high voltage, a value of $5 \times 10^{-16}\,\mathrm{C^4\,s^4\,m^{-6}\,kg^{-2}}$ is assumed for A. The resulting specific charge for the range of applied emitter voltages is shown in Fig. 7. The value assumed for A is likely specific to the emitter configuration and working fluid investigated here. Equation 38 is consistent with the conclusion from Courtney and Shea, that the specific charge increases with the negative Laplace pressure of the reservoir.[10] Decreasing the reservoir pore size increases the magnitude of the restorative pressure provided by the reservoir, raising the startup voltage of the device and decreasing the emitted flow rate through Eq. 21; the increased electric field required for emission significantly increases the charge concentration on the Taylor cones from which the species are emitted.

A porous reservoir provides a restorative force to the fluid upstream of the emitter. The Laplace pressure provided by the porous reservoir is characterized by the largest wetted pores in the medium. Porous materials designated P0 (160-250 µm), P1 (100-160 µm), P2 (40-100 µm), and P3 (16-40 µm) per ISO

4793 are considered for use as porous reservoirs. Porous materials of grades P0, P1, P2, and P3 are simplified as being characterized by uniform pore diameters of 180, 100, 70, and 45 µm respectively. Within the emitter substrate, formed from P5 (1.0-1.6 µm) porous material, the pressure is above the restorative pressure from the characteristic pore size (−136 kPa), so the pressure in the emitter is not limited by the emitter pore size. For the range of applied voltage in this study, the effect of emitter pore size is ignored.

Typically, porous permeability is determined by measuring the flow rate through a porous sample under an applied pressure difference. In lieu of experimental measurements or manufacturer specifications, the porous permeability of the P5-grade porous frit used as the emitter material is estimated to be 10^{-15} m^2 for the predicted total emitter current to match with experimental results. This value has order of magnitude agreement with the porous permeability inferred from manufacturer data for porous frits manufactured by Robu of the same porosity grade.[37] From the manufacturer data for driving pressure and flow rate, rearranging Darcy's law provides a porous permeability of $k = 6 \times 10^{-15}$ m^2 for P5-grade porous material from Robu.

VI. RESULTS AND DISCUSSION

The procedure for modeling the operation of the electrospray emitter is as follows. First, using Eq. 21 and the experimental properties of the device (i.e. emitter geometry[10] and propellant properties for EMI-BF4[38]), the total current from the device is determined and shown in Fig. 8. The specific charge is determined using Eq. 38. The emission site spacing is then obtained analytically with the small angle approximation using Eq. 36 and iteratively without the small angle approximation; these results are plotted in Fig. 9. Comparison of the exact and small angle approximation (used to determine Eq. 31) solutions for emission site spacing show that the two are in approximate agreement. This entire process is repeated for each porous reservoir of interest, using the associated characteristic pore size to determine the Laplace pressure supplied by the reservoir. The Laplace pressure of the reservoir is then ignored to determine the site spacing for the case of an open reservoir, indicated as *No Res.* in Figs. 9 and 10. Finally, the current of each emission site is determined using Eq. 20 and plotted in Fig. 10.

While this effort assumes that the system is 2D and homogeneous, the physical device is not so. For example, the emission surface is assumed to be smooth and well-described by a 2D geometry, whereas the fabricated emitter has variation in the sharpness along the length of the emitter. Variations in sharpness will create electric field concentration points that will produce electrospray emission below the predicted startup voltage. Additionally, because porous permeability is a macroscopic property, any anisotropy or nonhomogeneity is ignored. The scale over which porous permeability is determined is much larger than the emission site spacing, so uncharacterized nonhomogeneity may have a strong effect on the fluid flow cells. It is expected that the divergence of predicted results from experimental data at voltages close to the startup voltage is due to simplifications such as these, i.e. the nonhomogeneity of the device that is ignored in the model.

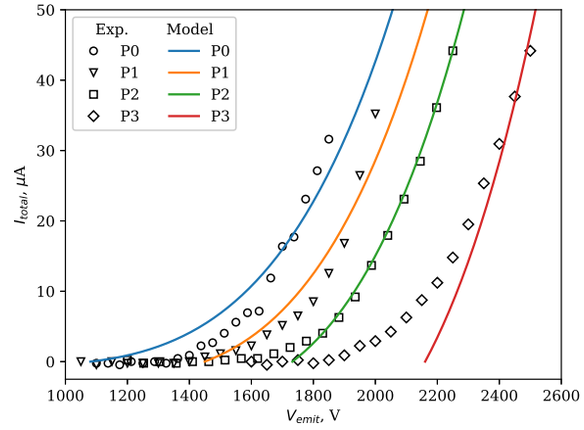

FIG. 8: The total current produced by the device as a function of emitter voltage and reservoir grade. Results from the presented model are shown with experimental results from Courtney and Shea.[10] Experimental results reproduced from [Appl. Phys. Lett. 107, 103504 (2015); doi: 10.1063/1.4930231], with the permission of AIP Publishing.

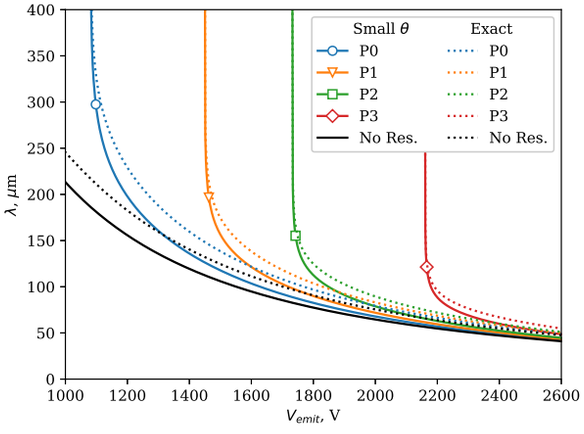

FIG. 9: The distance between adjacent emission sites with varying reservoir grade and with no reservoir, with and without using the small angle approximation for the secondary electric field to determine Eq. 31.

Predicted results for emission site spacing match well with *ex situ* estimation from Courtney et al.[13] of "a few emission sites [...] per 100 µm of length." For total currents above a few µA, the predicted emission site spacing is below 250 µm, showing that $\lambda \ll 2.56$ mm to neglect F_2 to simplify Eq. 14 is a valid assumption.

After determining the site spacing and individual emission site current, the contributions to the secondary electric

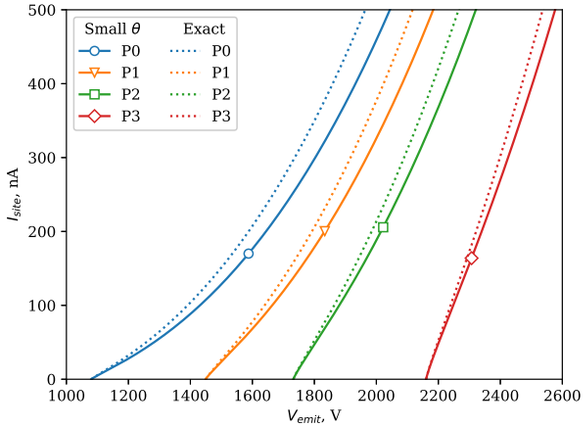

FIG. 10: The current emitted by each emission site, with and without using the small angle approximation for the secondary electric field to determine Eq. 31.

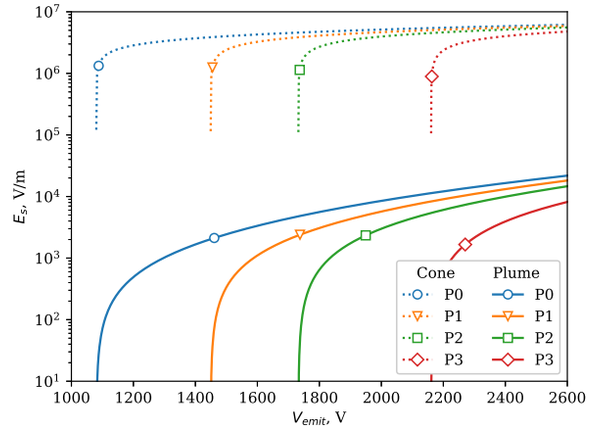

FIG. 11: Comparison of the secondary electric field produced by cones and plumes at the midpoint between emission sites.

field from the plume and cone were calculated and shown in Fig. 11. For all voltages and reservoir configurations, the contribution from the cone was over 500 times that of the contribution from the plume. As $E_{s,1}/E_{s,2} < 0.2\%$, neglecting the electric field from the plume to simplify Eq. 30 is valid. While the emitted particles were assumed to be ejected from the emission surface at their final velocity for this study, considering the acceleration of particles as they travel downstream would increase the contribution of the electric field from the plume. The electric field solution in Fig. 4 showed that the local electric potential decreases to 70% of the emitter potential within 25 µm of the emitter surface, which is less than half the smallest site spacings predicted for the modeled conditions. Through conservation of energy, it can be estimated that emitted particles reach roughly 55% of their final velocity within the first 25 µm downstream of the emitter. Because the linear charge density assumed to represent the plume scales with the inverse of particle velocity per Eq. 24, approximating the plume as a collection of particles at their final velocity only underestimated the electric field contribution of the plumes by a factor of 2 at most. Taking this factor into account raises the contribution of the electric field from the plume to less than 0.5% of that from the cones, so neglecting the electric field from the plume is valid.

Figure 12 shows the pressure and fluid velocity near the emission surface at the emitter. The effect of the secondary flow is generally limited to within the region of $r < \lambda$. In a physical device, small-scale spatial variation in porous permeability in this region may have a large effect on the secondary flow. The hydraulic pressure drop associated with the secondary flow was used in Eq. 33 to determine the emission site spacing; a spatially-varying porous permeability would violate the homogeneous assumption used to describe the porous flow in this effort. To account for heterogeneity in the medium on the order of the site spacing, the right side of Eq. 36 may be multiplied by $\hat{k}^{-1}$, where $\hat{k}$ represents the local porous permeability normalized by the mean porous permeability. In this way, localized variation in porous permeability near the emission surface may be the cause of spatially nonuniform emission that has been observed experimentally.[18,19]

To investigate the low Reynolds number assumption for simplifying Darcy's law, the maximum flow velocity in the porous medium is determined. The maximum flow velocity always occurs at the pressure wells of the emission sites, where the primary and secondary flows are equal and additive; the fluid velocity here is twice the primary flow velocity at the emission surface from Eq. 2. The maximum Reynolds number in the porous medium is then solved as:

$$Re = \frac{2I_{site}}{\rho\theta_w R_2 \lambda}\frac{m}{q}\frac{\rho d}{\mu} = \frac{2I_{site} d}{\mu\theta_w R_2 \lambda}\frac{m}{q}, \tag{39}$$

where d is taken as the characteristic pore size for the emitter substrate: 1.0 to 1.6 µm; in lieu of information about the particle size in the porous medium, the particle size is assumed to be similar to the characteristic pore size. The Reynolds number for flow in the porous medium is below 10^{-6} for all the presented results, so the low Re assumption is valid.

By enforcing a stagnation point, the emission site spacing expands and contracts in response to changes in the primary flow rate. Emission site expansion is accompanied by a corresponding decrease in the secondary flow fluid velocity to account for the decreased primary flow rate. In lieu of a full stability analysis, the stagnation point condition between emission sites is sufficient.

Results from this effort may inform experimental results for porous electrospray emitters of different geometries in the mass spectrometry community, for example where nonlinear increases in total current have been observed with increasing emitter voltage.[39,40]

To further simplify Eq. 21, the specific charge can be substituted by Eq. 38 and a parameter S can be introduced to represent the hydraulic resistance for the primary flow to the emis-

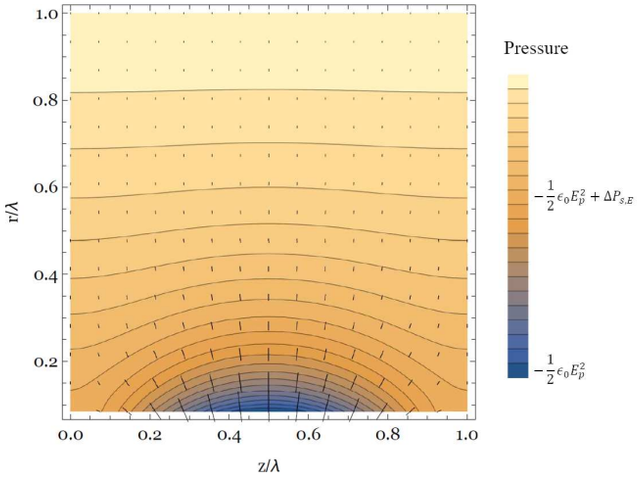

FIG. 12: Generalized results for pressure in 1 emission cell, with the emission surface along the horizontal axis. Superposed line segments represent the flow direction and magnitude.

sion surface:

$$I_{total} \approx \frac{AE_p^3 \Delta P_{app}}{S\gamma}; \qquad S = \frac{\mu \ln\left(\frac{R_2}{R_1}\right)}{k\theta_w L}. \tag{40}$$

From this relation we see that the total emission current, I_{total}, is inversely proportional to the primary flow hydraulic resistance, which we designate as the wedge hydraulic resistance S, with units of Pa s m^{-3}. The effects that fluid properties and geometry have on the specific charge coefficient A require further investigation. The effect that the wedge angle θ_w has on the electric field via the electric field to voltage coefficient C_E must be considered, even though Eq. 40 suggests that I_{total} is proportional to the wedge angle.

This model provides insight into how a porous emitter generally responds to operational and design changes; however, more accurate representation requires further investigation into the assumptions and approximations made in developing this model. For example, emission sites were assumed to lie on the midplane of the emitter, experimental evidence however suggests that emission sites may be oriented about 10° from midplane.[13] The secondary flow, in particular, would benefit from a 3-dimensional representation of the flow near each emission site. For a more accurate representation of the secondary electric field, charge in the plume and the shape and charge distribution at a porous electrospray site should be considered. A more general solution for $P(r,z)$ as derived in Appendix I will be more useful for cases where the emission site spacing is large. For example, in wedge geometries where the radius to the base of the wedge R_1 is small, the emission site spacing λ may be comparable to R_1 over the entire operating range of the device. In these cases, the assumption $\lambda \ll 2\pi R_1$ cannot be made.

VII. CONCLUSION

This study develops an analytical model that provides intuitive and useful relationships for understanding the total current and emission site spacing for linear porous wedge electrospray emitters. By considering an equilibrium of the effects from Coulomb repulsion and the subsurface pressure variation, quantitative descriptions (i.e. through Eqs. 10 and 36) provide insight into the effects that fluid properties, emitter geometry, and porous media properties have on the behavior and performance of such devices. This analysis leads to the conclusion that the wedge hydraulic resistance, as defined in Eq. 40, is adequate for understanding the total output for the investigated geometry. An explanation for the variation in the specific charge of plume constituents is proposed through Eq. 38. Quantitative evaluation of the porous flow leads to Eq. 21 and the conclusion that the secondary flow can be ignored only to predict the total current for the considered geometry.

ACKNOWLEDGMENTS

The authors would like to thank Daniel Courtney and Nathaniel Demmons for their insightful discussions throughout the years. This work was supported by NASA Space Technology Research Fellowship grant #80NSSC18K1194.

DATA AVAILABILITY

The data that support the findings of this study are available within the article.

VIII. APPENDIX I

Supposing that the emission site spacing may not be small compared to the radius of the wedge base, a more general solution for the pressure in the wedge is sought. For this case, we consider a secondary flow which satisfies the following boundary conditions in r:

$$P_s(R_1,z) = 0, \quad P_s(R_2,z) = \hat{P}e^{i\alpha z}. \tag{A1}$$

where $\hat{P}$ is a constant to represent the magnitude of pressure variation at the emission surface, $r = R_2$. The solution to Laplace's equation in this case is similar to Eq. 5:

$$P_s(r,z) = \hat{P}\left[\hat{C}_2 K_0(\alpha r) + \hat{C}_3 I_0(\alpha r)\right] e^{i\alpha z} \tag{A2}$$

where $\hat{C}_2$ and $\hat{C}_3$ are constant coefficients. Solving for the given boundary conditions yields:

$$\hat{C}_2 = -\frac{\frac{I_0(\alpha R_1)}{K_0(\alpha R_1)}}{I_0(\alpha R_2) - \frac{I_0(\alpha R_1)}{K_0(\alpha R_1)} K_0(\alpha R_2)}, \tag{A3}$$

$$\hat{C}_3 = \frac{1}{I_0(\alpha R_2) - \frac{I_0(\alpha R_1)}{K_0(\alpha R_1)} K_0(\alpha R_2)} \tag{A4}$$

The pressure within the wedge is given by the superposition of the primary and secondary flows:

$$P(r,z) = \frac{P_0 \ln\left(\frac{r}{R_2}\right)}{\ln\left(\frac{R_1}{R_2}\right)} + \hat{P}\left[\hat{C}_2 K_0(\alpha r) + \hat{C}_3 I_0(\alpha r)\right] e^{i\alpha z}, \tag{A5}$$

where P_0 is the pressure at R_1 relative to the mean pressure at R_2. The flow field is then solved through Darcy's law, where $\vec{u} = -\frac{k}{\mu}\nabla P$:

$$u_r = -\frac{kP_0}{\mu r \ln\left(\frac{R_1}{R_2}\right)} - \frac{2\pi k\hat{P}}{\mu\lambda}\left[-\hat{C}_2 K_1(\alpha r) + \hat{C}_3 I_1(\alpha r)\right] e^{i\alpha z}, \tag{A6}$$

$$u_z = i\frac{2\pi k\hat{P}}{\mu\lambda}\left[\hat{C}_2 K_0(\alpha r) + \hat{C}_3 I_0(\alpha r)\right] e^{i\alpha z}. \tag{A7}$$

Integrating u_r over the base of the base of the wedge at R_1 yields the total flow rate, Q:

$$Q = \frac{kP_0\theta_w L}{\mu \ln\left(\frac{R_1}{R_2}\right)} + \frac{ik\hat{P}}{\mu}\left[-\hat{C}_2 K_1(\alpha R_1) + \hat{C}_3 I_1(\alpha R_2)\right]\left(1 - e^{i\alpha L}\right). \tag{A8}$$

To solve for $\hat{P}$, the radial flow is solved at stagnation points on the emission surface, R_2. Stagnation points exist at the maxima of the secondary flow pressure on the emission surface, $(r,z) = (R_2, n\lambda)$ where n is an integer. Solving Eq. A6 for these condition yields:

$$-\frac{P_0}{R_2 \ln\left(\frac{R_1}{R_2}\right)} - \frac{2\pi\hat{P}}{\lambda}\left[-\hat{C}_2 K_1(\alpha R_2) + \hat{C}_3 I_1(\alpha R_2)\right] = 0, \tag{A9}$$

Rearranging terms yields an equation for $\hat{P}$:

$$\hat{P} = -\frac{\lambda P_0}{2\pi R_2 \ln\left(\frac{R_1}{R_2}\right)}\left[-\hat{C}_2 K_1(\alpha R_2) + \hat{C}_3 I_1(\alpha R_2)\right]^{-1}. \tag{A10}$$

P_0 is then solved for by applying the Maxwell pressure and the reservoir Laplace pressure conditions to the flow.

[1] C. Byon, S. Ku, W. Lee, J. H. Jung, and W. Kim, "Electrospray characterization based on an emitter of cone-shaped porous medium for the high-throughput microliter aerosol generation," Applied Physics Letters **111**, 123504 (2017).
[2] T. Koerner, K. Turck, L. Brown, and R. D. Oleschuk, "Porous polymer monolith assisted electrospray," Analytical chemistry **76**, 6456–6460 (2004).
[3] R. Legge, P. Lozano, and M. Martinez-Sanchez, "Fabrication and characterization of porous metal emitters for electrospray thrusters," in *International Electric Propulsion Conference* (ERPS, 2007) p. 145.
[4] M. R. Natisin and H. L. Zamora, "Performance of a fully conventionally machined liquid-ion electrospray thruster operated in pir," in *International Electric Propulsion Conference* (ERPS, 2019) p. 522.
[5] D. G. Courtney, H. Q. Li, and P. Lozano, "Emission measurements from planar arrays of porous ionic liquid ion sources," Journal of Physics D: Applied Physics **45**, 485203 (2012).
[6] Y. Guo, S. Li, Z. Wu, Y. Hen, and Z. Sun, "Study on performance of ionic liquid electrospray thruster in atmospheric and vacuum environment," in *International Electric Propulsion Conference* (ERPS, 2019) p. 559.
[7] C. Ma, T. Bull, and C. Ryan, "Feasibility study of a micro-electrospray thruster based on a porous glass emitter substrate," in *International Electric Propulsion Conference* (ERPS, 2017) p. 485.
[8] X. Liu, W. He, X. Kang, and M. Xu, "Fabrication of porous emitters for ionic liquid ion source by wire electrical discharge machining combined with electrochemical etching," Review of Scientific Instruments **90**, 123304 (2019).
[9] R. J. Antypas and J. J. Wang, "Pure ionic electrospray extractor design optimization," in *International Electric Propulsion Conference* (ERPS, 2019) p. 372.
[10] D. G. Courtney and H. Shea, "Influences of porous reservoir laplace pressure on emissions from passively fed ionic liquid electrospray sources," Applied Physics Letters **107**, 103504 (2015).
[11] N. R. Demmons, Z. Wood, and N. Alvarez, "Characterization of a high thrust, pressure-fed electrospray thruster for precision attitude control applications," in *Propulsion and Energy Forum* (AIAA, 2019) p. 3817.
[12] D. Spence, E. Ehrbar, N. Rosenblad, N. Demmons, T. Roy, S. Hoffman, W. D. Williams, M. Tsay, J. Zwahlen, K. Hohman, *et al.*, "Electrospray propulsion systems for small satellites and satlets," in *SPACE 2013 Conference and Exposition* (AIAA, 2013) p. 5329.
[13] D. G. Courtney, S. Dandavino, and H. Shea, "Comparing direct and indirect thrust measurements from passively fed ionic electrospray thrusters," Journal of Propulsion and Power **32**, 392–407 (2015).
[14] B. Little and M. Jugroot, "Bimodal propulsion system for small spacecraft: Design, fabrication, and performance characterization," Journal of Spacecraft and Rockets , 1–13 (2020).
[15] C. Chen, M. Chen, and H. Zhou, "Characterization of an ionic liquid electrospray thruster with a porous ceramic emitter," Plasma Science and Technology (2020).
[16] D. Courtney, N. Demmons, and P. Wright, "Colloid thruster and method," (2017), uS Patent 9,638,178.
[17] C. Guerra-Garcia, D. Krejci, and P. Lozano, "Spatial uniformity of the current emitted by an array of passively fed electrospray porous emitters," Journal of Physics D: Applied Physics **49**, 115503 (2016).
[18] D. G. Courtney, Z. Woods, and T. Fedkiw, "Reconstructing electrospray plume current spatial distributions using computed tomography," in *International Electric Propulsion Conference* (ERPS, 2019) p. 787.
[19] C. Chen, M. Chen, W. Fan, and H. Zhou, "Effects of non-uniform operation of emission sites on characteristics of a porous electrospray thruster," Acta Astronautica **178**, 192 – 202 (2021).
[20] A. Thuppul, P. L. Wright, A. L. Collins, J. K. Ziemer, and R. E. Wirz, "Lifetime considerations and estimation for electrospray thrusters," Aerospace **7**, 108 (2020).
[21] J. Bear, *Dynamics of fluids in porous media* (Courier Corporation, 2013).
[22] S. M. Hassanizadeh and W. G. Gray, "Thermodynamic basis of capillary pressure in porous media," Water resources research **29**, 3389–3405 (1993).
[23] D. P. Smith, "The electrohydrodynamic atomization of liquids," IEEE Transactions on Industry Applications , 527–535 (1986).
[24] C.-H. Chen, D. Saville, and I. A. Aksay, "Scaling laws for pulsed electrohydrodynamic drop formation," Applied Physics Letters **89**, 124103 (2006).
[25] G. I. Taylor, "Disintegration of water drops in an electric field," Proceedings of the Royal Society of London. Series A. Mathematical and Physical Sciences **280**, 383–397 (1964).
[26] J. D. Jackson, *Classical electrodynamics* (John Wiley & Sons, 2007).
[27] C. Coffman, M. Martínez-Sánchez, F. Higuera, and P. C. Lozano, "Structure of the menisci of leaky dielectric liquids during electrically-assisted evaporation of ions," Applied Physics Letters **109**, 231602 (2016).
[28] J. Fernández de La Mora, "The fluid dynamics of taylor cones," Annu. Rev. Fluid Mech. **39**, 217–243 (2007).
[29] C. S. Coffman, M. Martínez-Sánchez, and P. C. Lozano, "Electrohydrodynamics of an ionic liquid meniscus during evaporation of ions in a regime of high electric field," Physical Review E **99**, 063108 (2019).
[30] J. F. De La Mora, "On the outcome of the coulombic fission of a charged isolated drop," Journal of colloid and interface science **178**, 209–218 (1996).
[31] L. Rayleigh, "On the equilibrium of liquid conducting masses charged with electricity," The London, Edinburgh, and Dublin Philosophical Magazine

and Journal of Science **14**, 184–186 (1882).
[32]J. Peters, "Rayleigh's electrified water drops," European Journal of Physics **1**, 143 (1980).
[33]A. Gomez and K. Tang, "Charge and fission of droplets in electrostatic sprays," Physics of Fluids **6**, 404–414 (1994), https://doi.org/10.1063/1.868037.
[34]E. Davis and M. Bridges, "The rayleigh limit of charge revisited: light scattering from exploding droplets," Journal of aerosol science **25**, 1179–1199 (1994).
[35]I. Marginean, P. Nemes, L. Parvin, and A. Vertes, "How much charge is there on a pulsating taylor cone?" Applied Physics Letters **89**, 064104 (2006), https://doi.org/10.1063/1.2266889.
[36]K. Tang and R. D. Smith, "Theoretical prediction of charged droplet evaporation and fission in electrospray ionization," International journal of mass spectrometry **185**, 97–105 (1999).
[37]"Flowrate / pressure calculation vitrapor® - filterdiscs," http://www.adamschittenden.com/Robu%20flowrate%20graphs.pdf, accessed: 2019-09-01.
[38]Z.-B. Zhou, H. Matsumoto, and K. Tatsumi, "Structure and properties of new ionic liquids based on alkyl-and alkenyltrifluoroborates," ChemPhysChem **6**, 1324–1332 (2005).
[39]H. Wang, J. Liu, R. G. Cooks, and Z. Ouyang, "Paper spray for direct analysis of complex mixtures using mass spectrometry," Angewandte Chemie International Edition **49**, 877–880 (2010).
[40]G. Tepper and R. Kessick, "Nanoelectrospray aerosols from microporous polymer wick sources," Applied Physics Letters **94**, 084106 (2009).

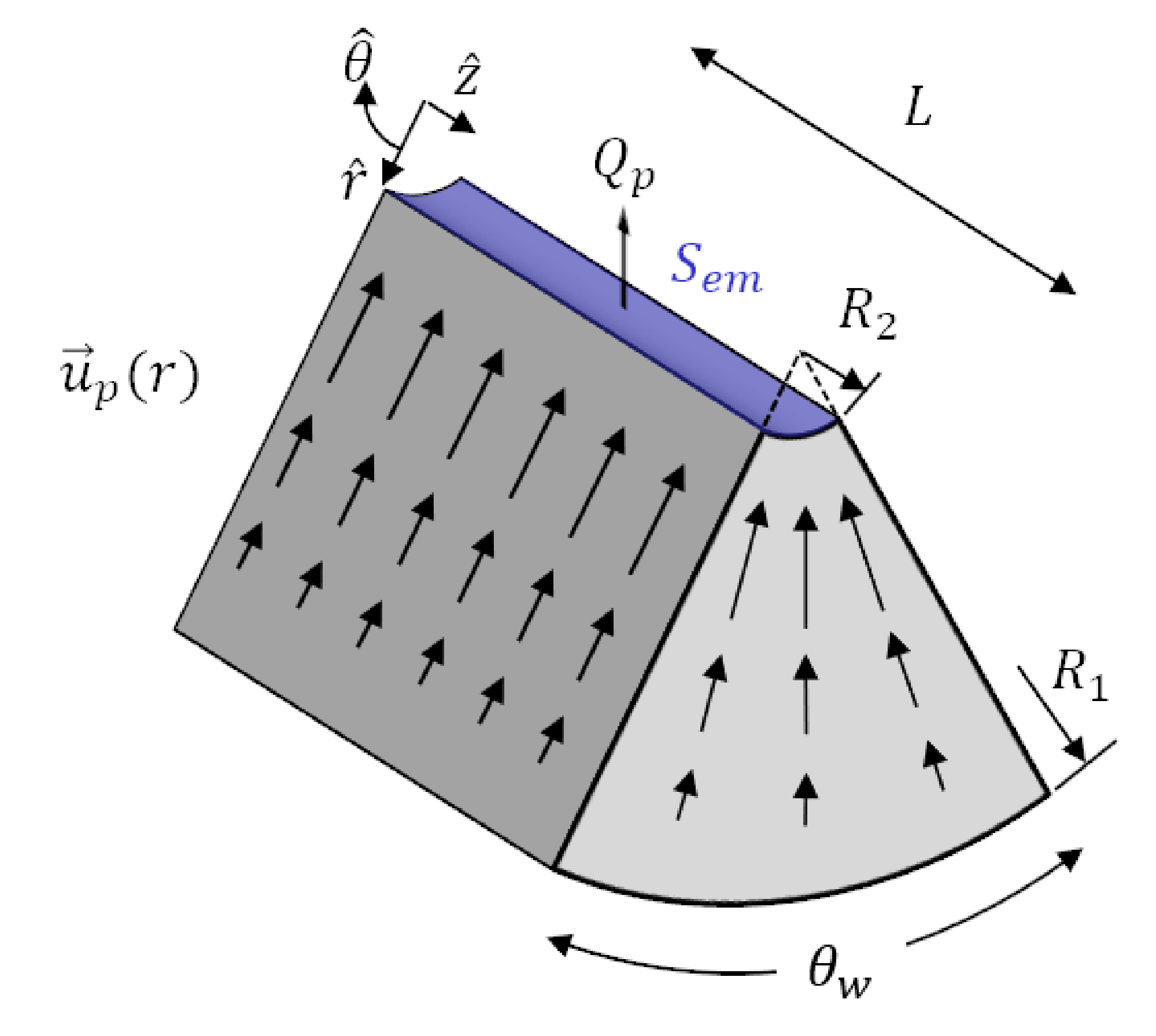
$\hat{\theta}$
$\hat{z}$
$\hat{r}$
L
Q_p
S_{em}
R_2
$\vec{u}_p(r)$
R_1
θ_w

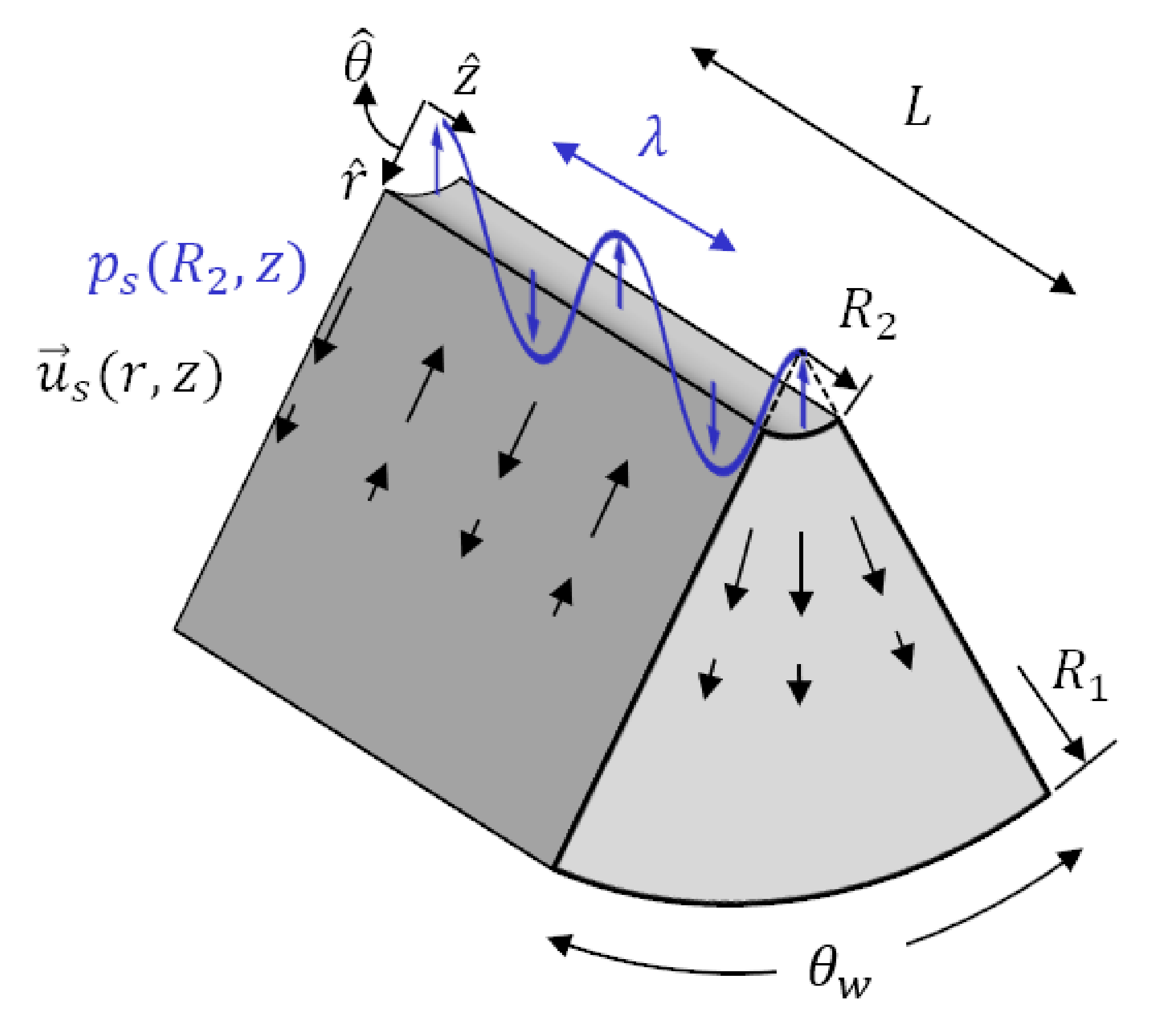
$\hat{\theta}$
$\hat{z}$
$\hat{r}$
λ
L
$p_s(R_2, z)$
$\vec{u}_s(r, z)$
R_2
R_1
θ_w

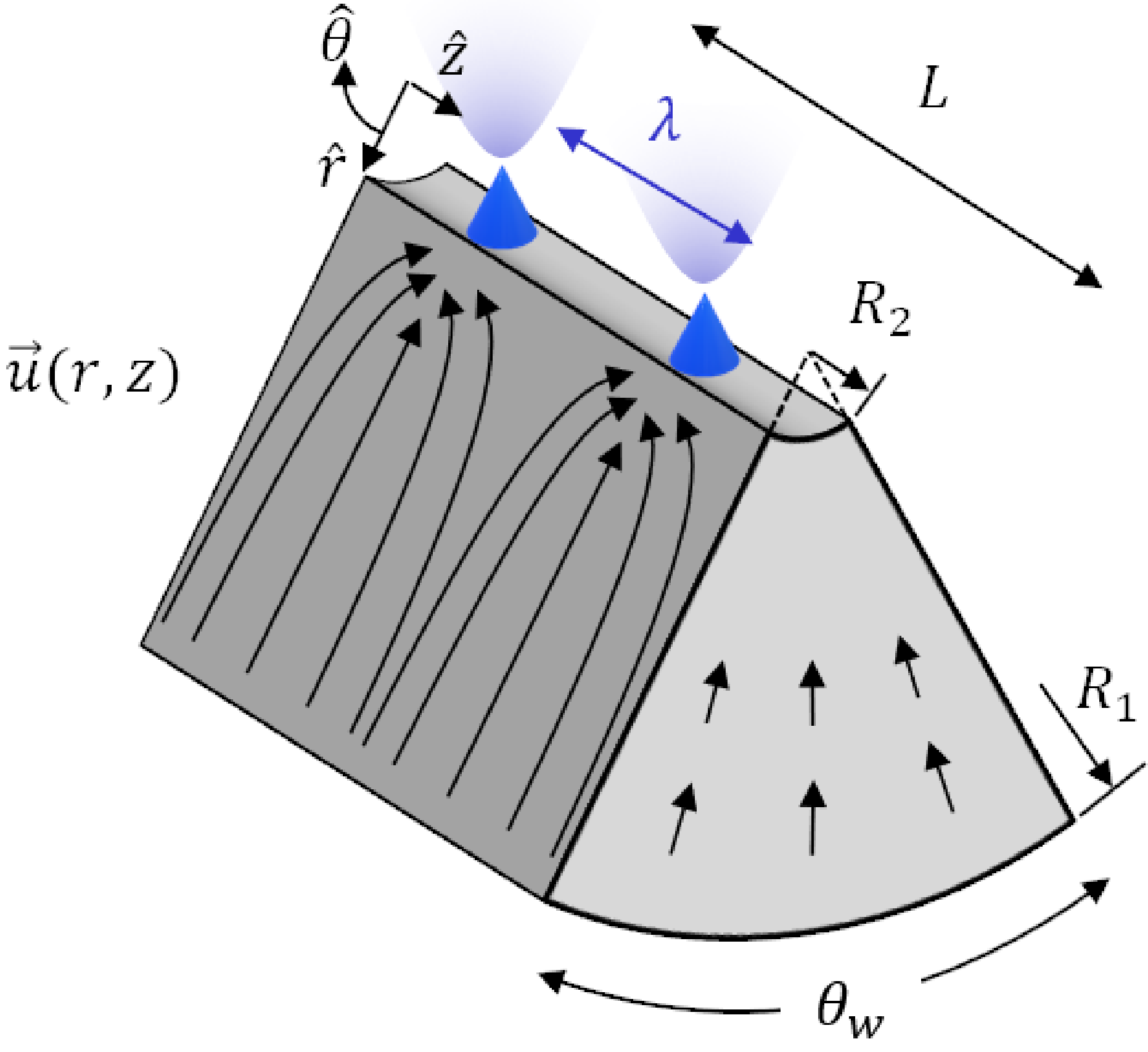
$\hat{\theta}$
$\hat{z}$
$\hat{r}$
λ
L
R_2
$\vec{u}(r,z)$
R_1
θ_w

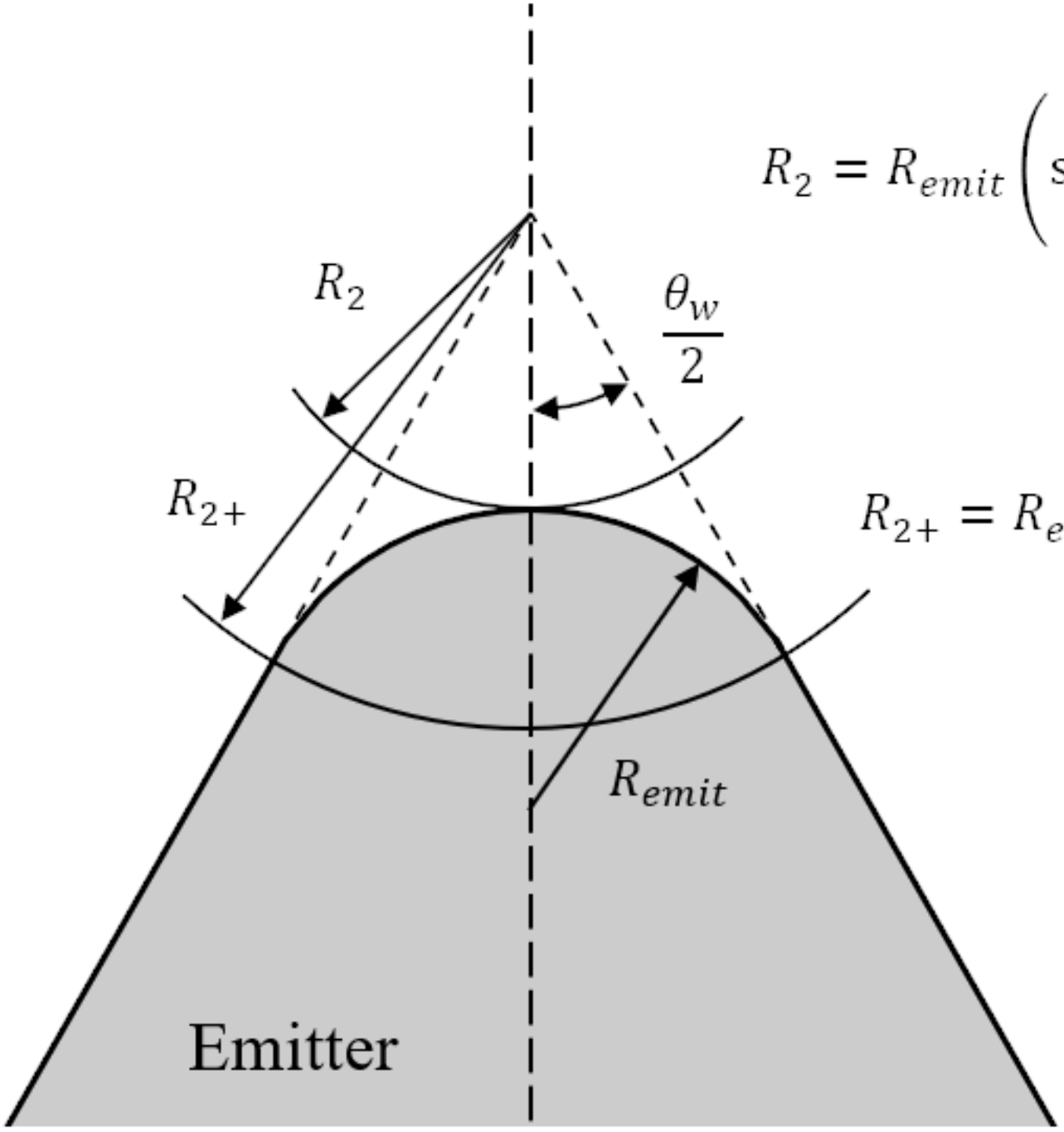

$$R_2 = R_{emit}\left(\sin\left(\frac{\theta_w}{2}\right)^{-1} - 1\right)$$

$$R_{2+} = R_{emit}\left(\sin\left(\frac{\theta_w}{2}\right)\right)^{-1}$$

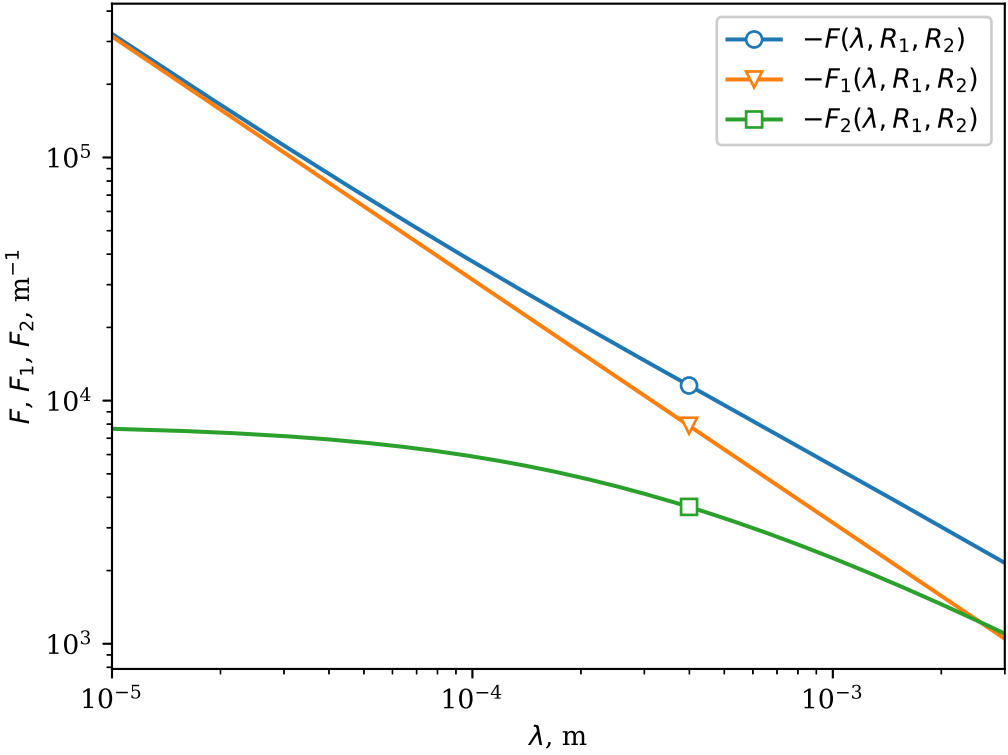
$-F(\lambda, R_1, R_2)$
$-F_1(\lambda, R_1, R_2)$
$-F_2(\lambda, R_1, R_2)$
10^5
10^4
10^3
F, F_1, F_2, m^{-1}
10^{-5}
10^{-4}
10^{-3}
λ, m

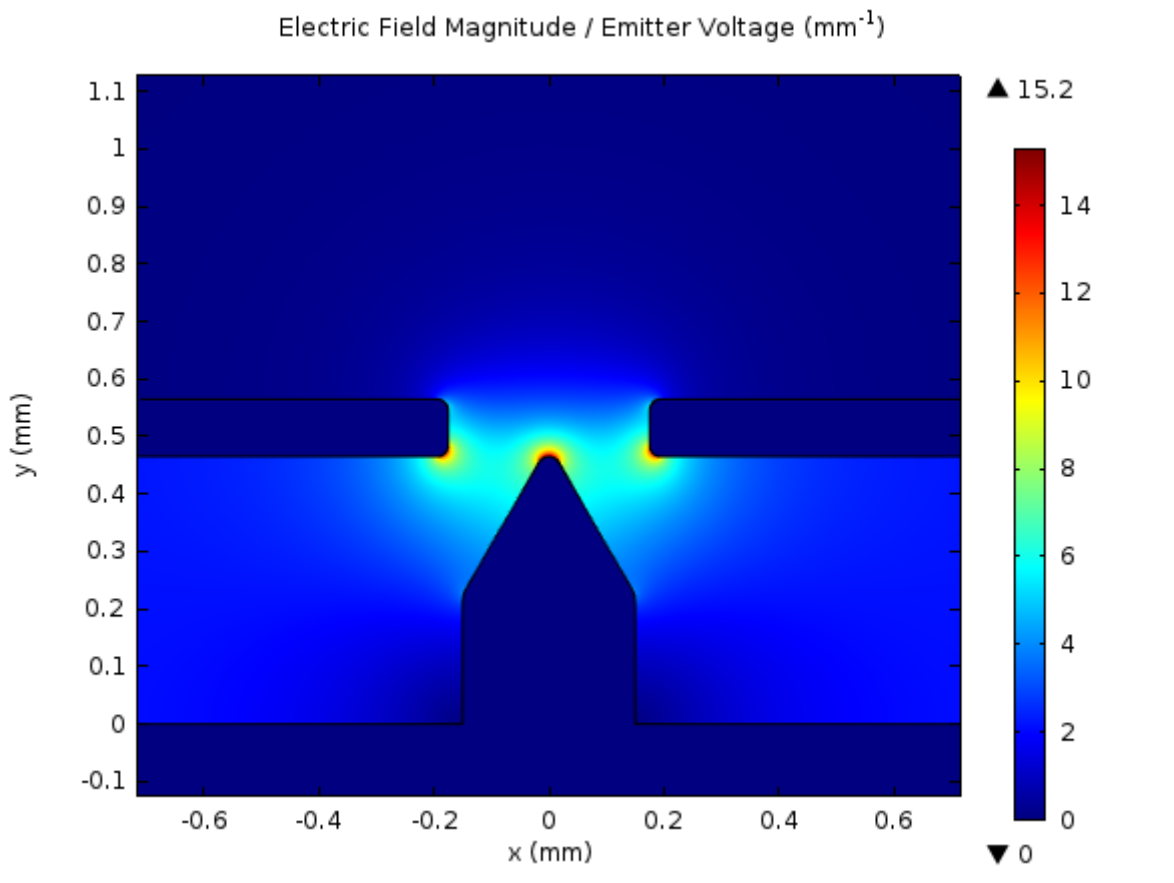
Electric Field Magnitude / Emitter Voltage (mm-1)
1.1
1
0.9
0.8
0.7
0.6
0.5
0.4
0.3
0.2
0.1
0
-0.1
y (mm)
-0.6
-0.4
-0.2
0
0.2
0.4
0.6
x (mm)
▲ 15.2
14
12
10
8
6
4
2
0
▼ 0

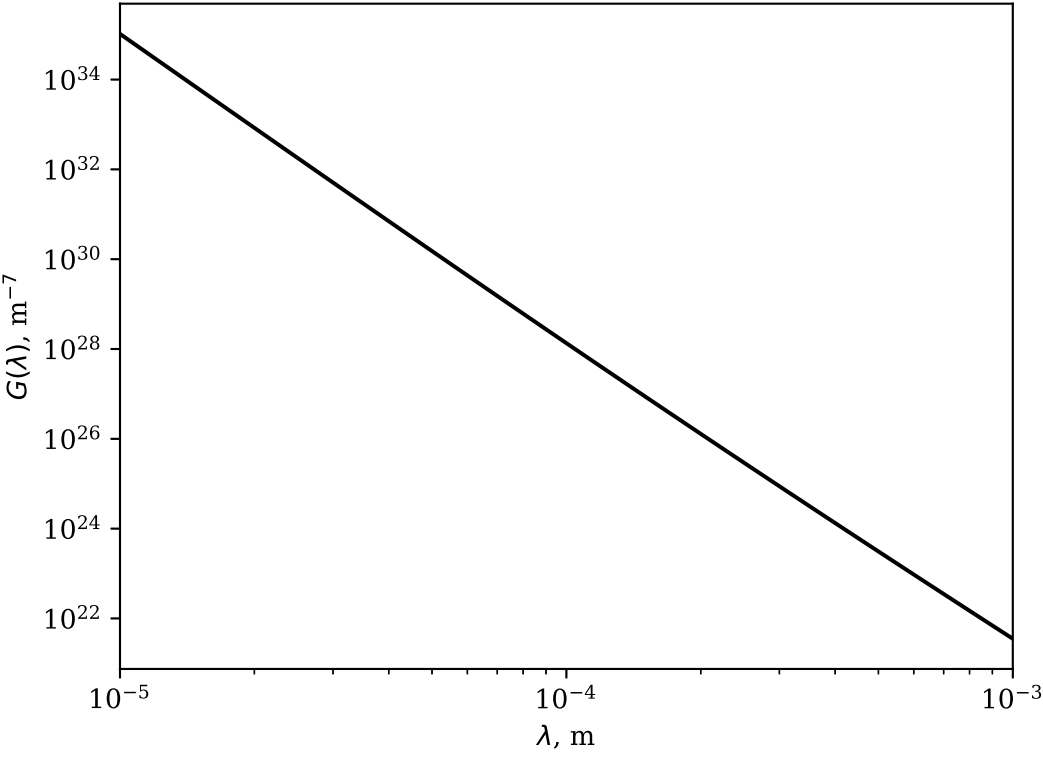
10^{34}
10^{32}
10^{30}
10^{28}
10^{26}
10^{24}
10^{22}
$G(\lambda)$, m^{-7}
10^{-5}
10^{-4}
10^{-3}
λ, m

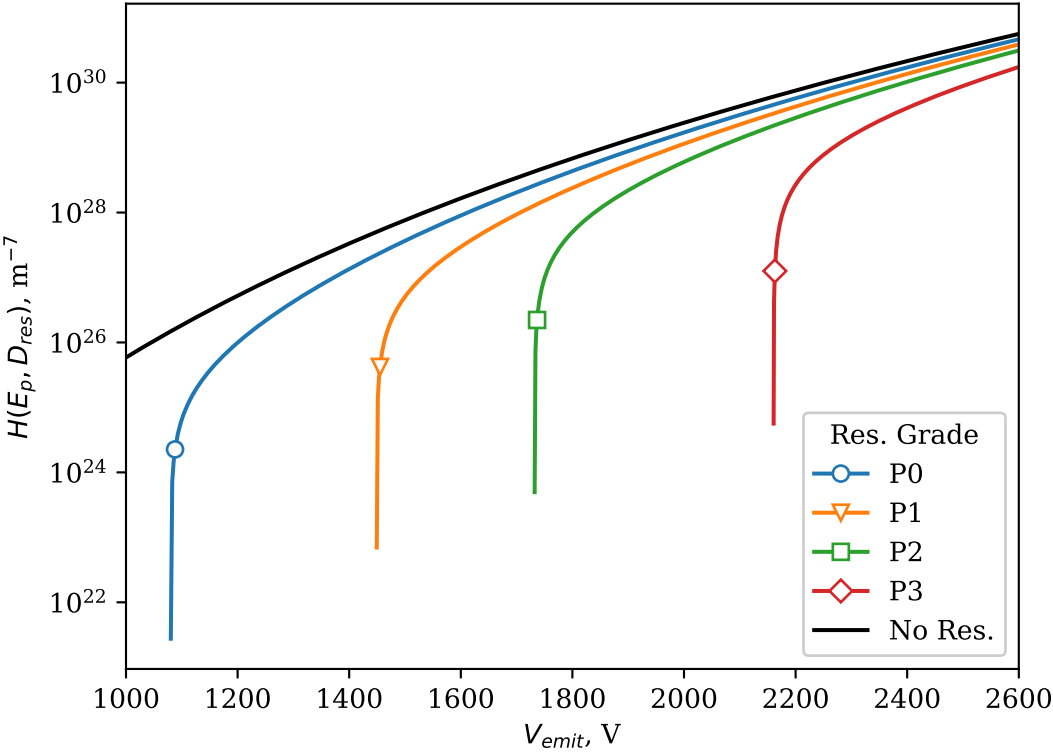
10^{30}
10^{28}
10^{26}
10^{24}
10^{22}
$H(E_p, D_{res})$, m^{-7}
1000
1200
1400
1600
1800
2000
2200
2400
2600
V_{emit}, V
Res. Grade
P0
P1
P2
P3
No Res.

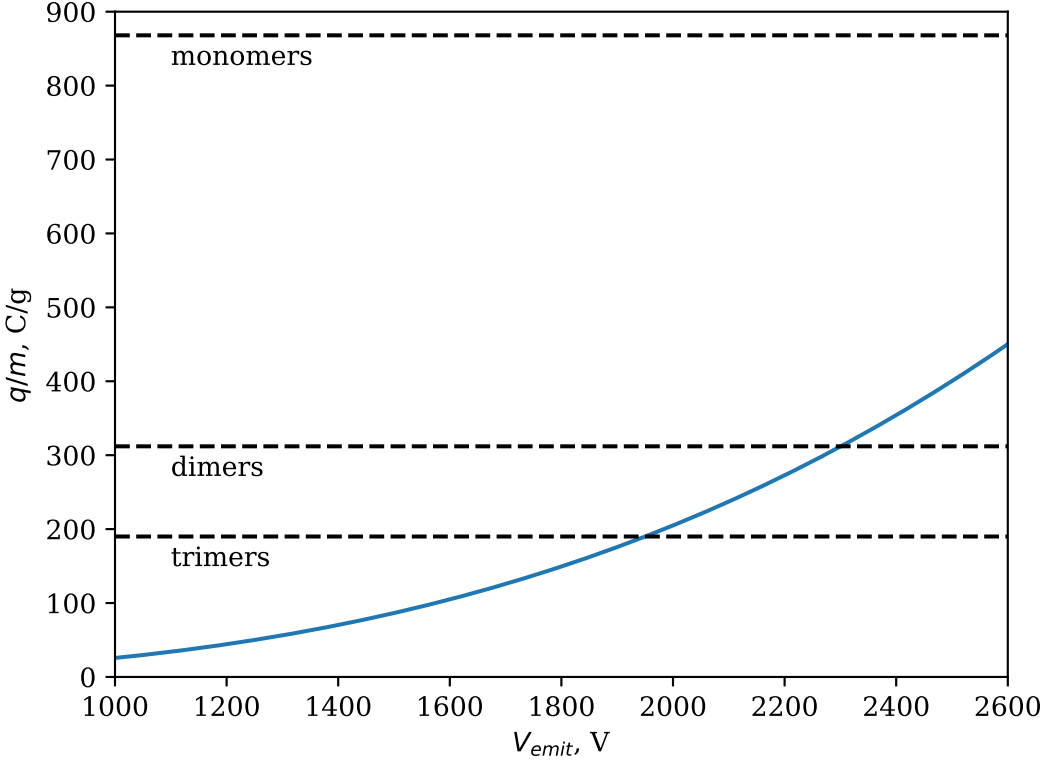
900
800
700
600
500
400
300
200
100
0
monomers
dimers
trimers
q/m, C/g
1000
1200
1400
1600
1800
2000
2200
2400
2600
V_{emit}, V

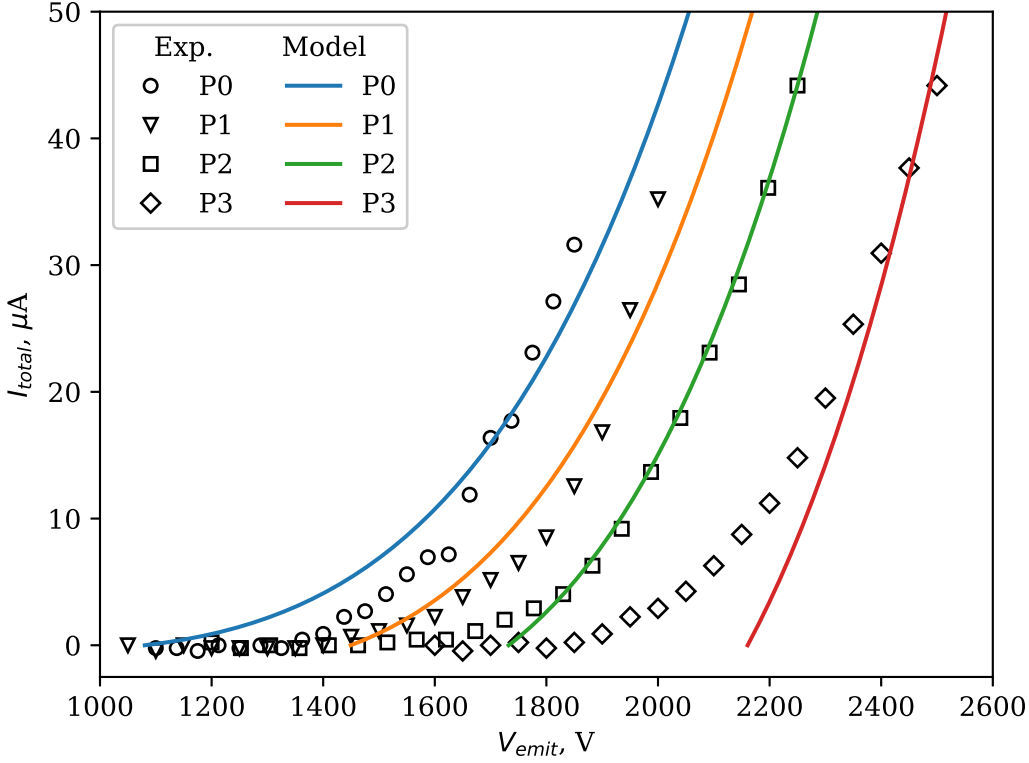
Exp.
Model
P0
P1
P2
P3
P0
P1
P2
P3
50
40
30
20
10
0
1000
1200
1400
1600
1800
2000
2200
2400
2600
I_{total}, μA
V_{emit}, V

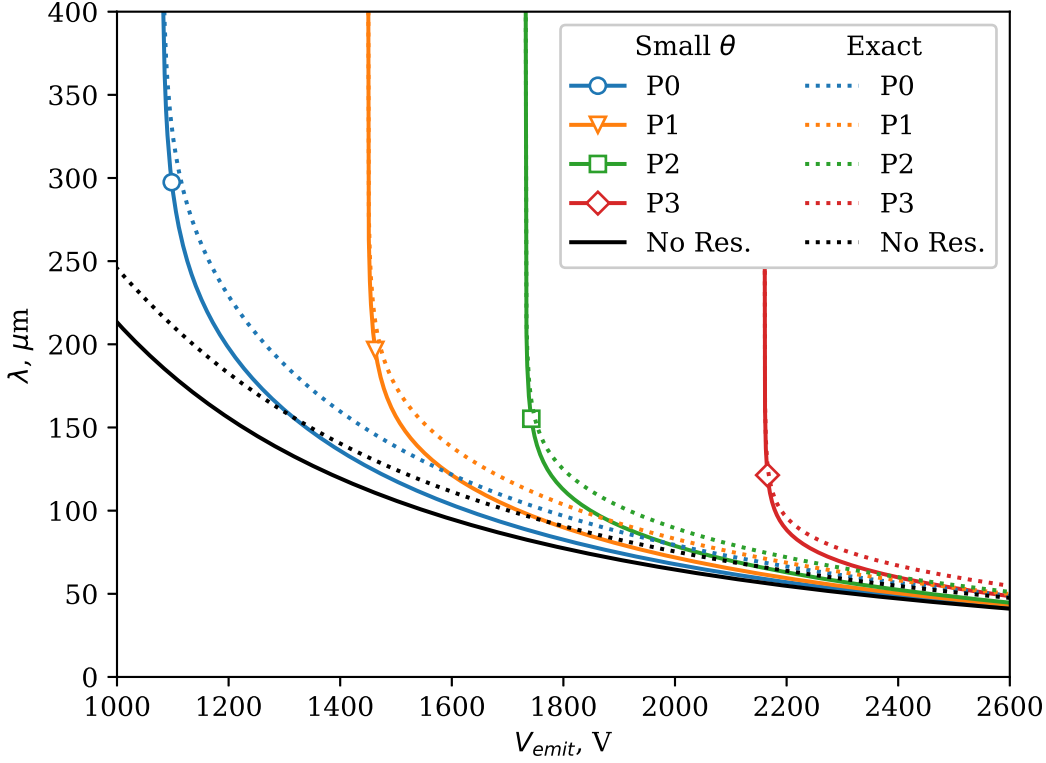
Small θ
Exact
P0
P1
P2
P3
No Res.
P0
P1
P2
P3
No Res.
λ, μm
V_{emit}, V
0
50
100
150
200
250
300
350
400
1000
1200
1400
1600
1800
2000
2200
2400
2600

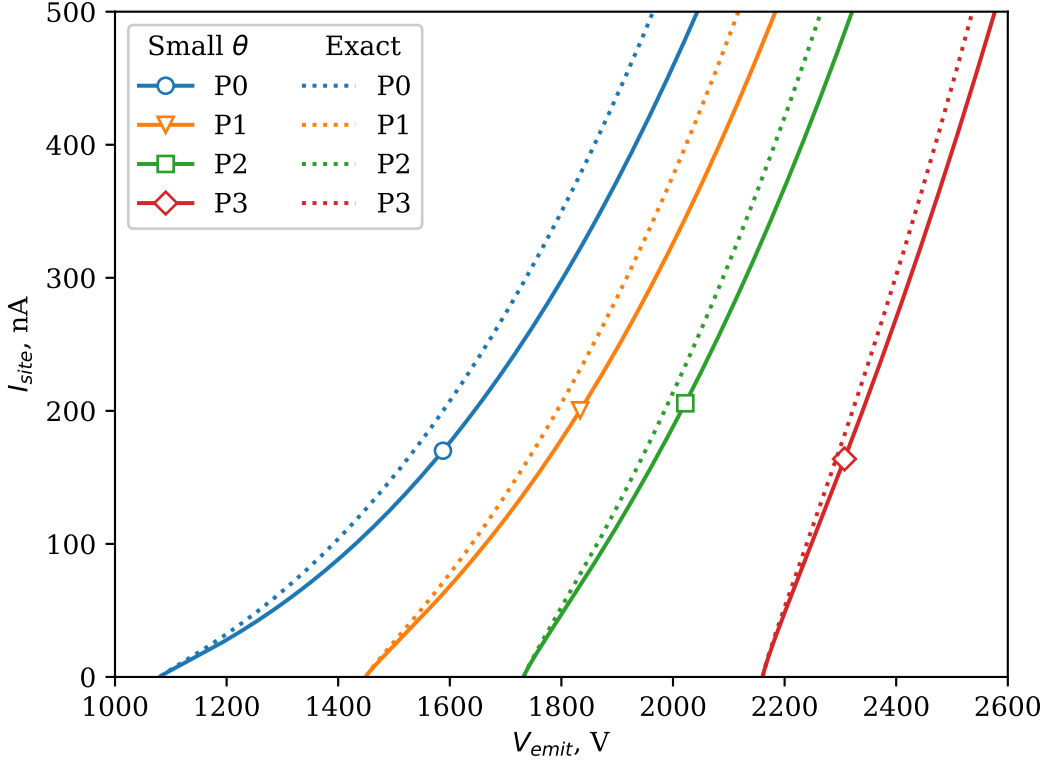
Small θ
Exact
P0
P1
P2
P3
P0
P1
P2
P3
500
400
300
200
100
0
1000
1200
1400
1600
1800
2000
2200
2400
2600
I_{site}, nA
V_{emit}, V

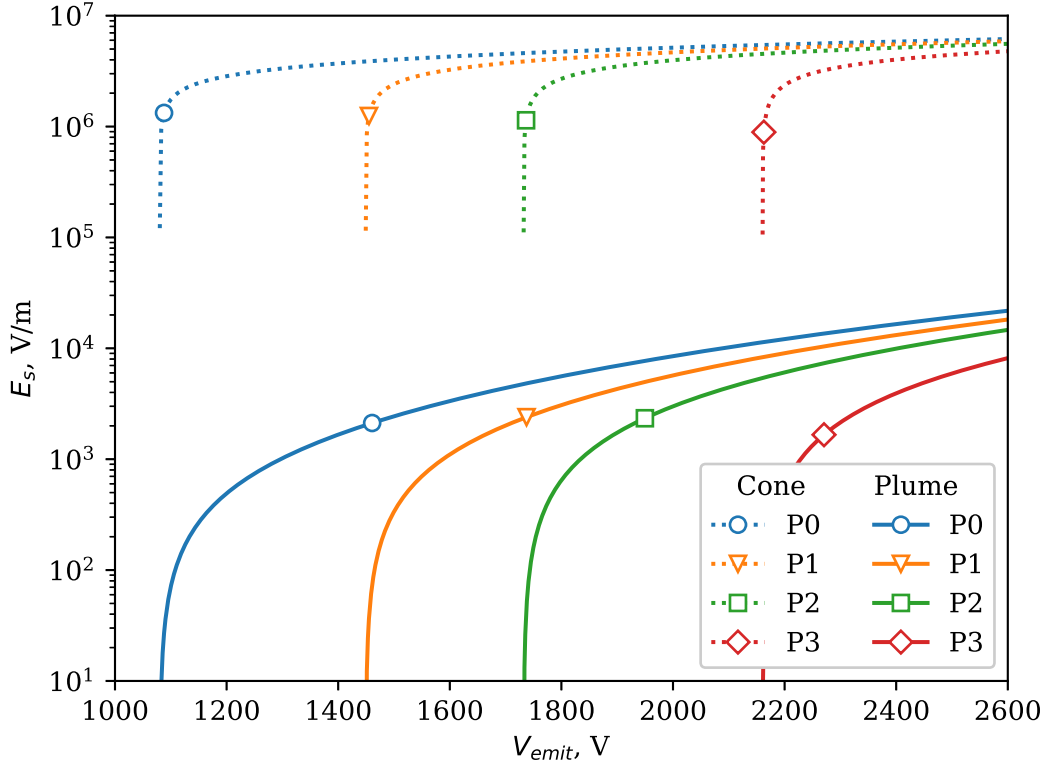
10^7
10^6
10^5
10^4
10^3
10^2
10^1
E_s, V/m
1000
1200
1400
1600
1800
2000
2200
2400
2600
V_{emit}, V
Cone
Plume
P0
P1
P2
P3
P0
P1
P2
P3

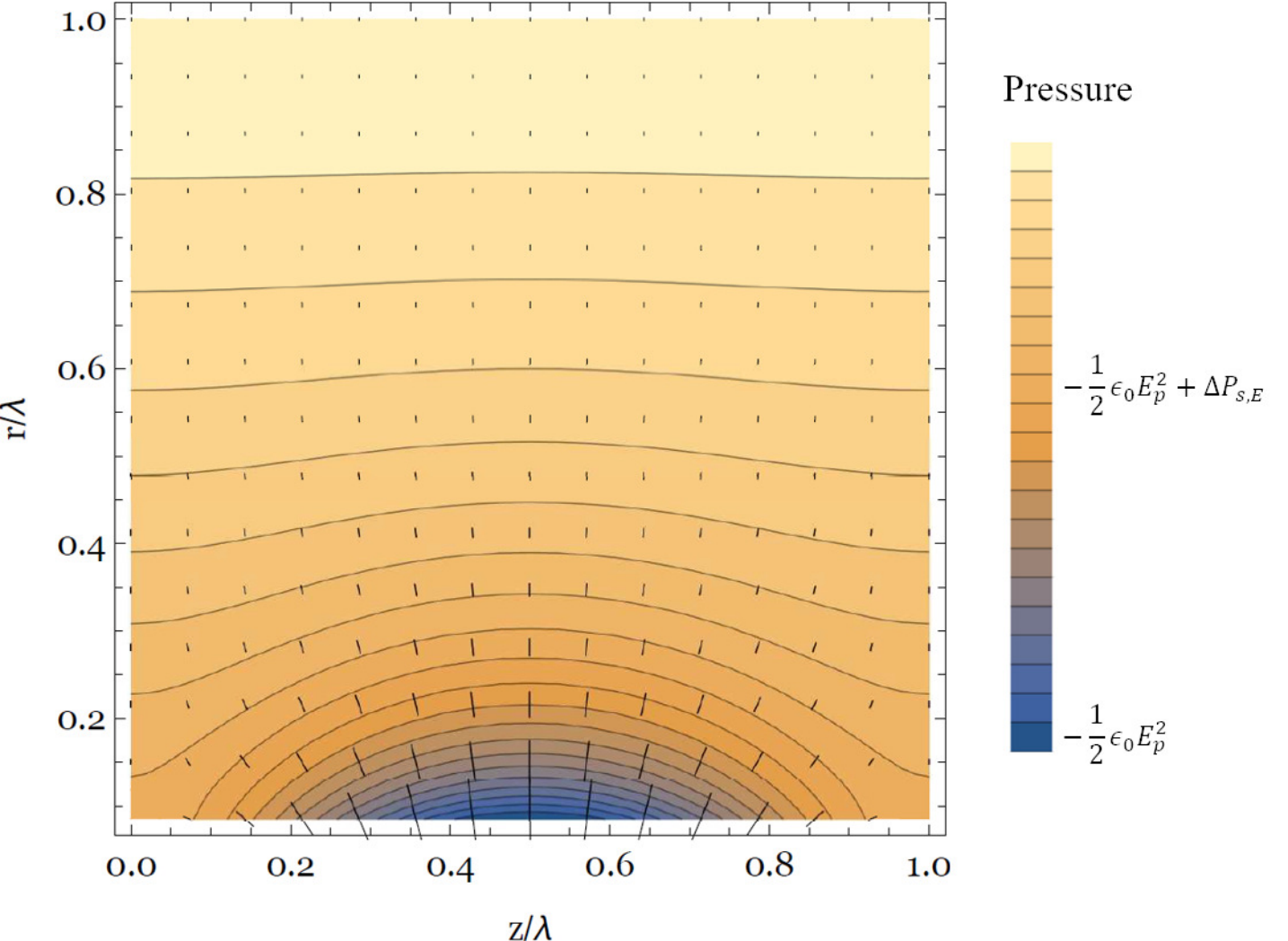
Pressure
$-\frac{1}{2}\epsilon_0 E_p^2 + \Delta P_{s,E}$
$-\frac{1}{2}\epsilon_0 E_p^2$
r/λ
z/λ
0.0
0.2
0.4
0.6
0.8
1.0